Aperiodic Nanoplasmonic Devices for Directional Colour Filtering and Sensing

Matthew S. Davis[1, 2, 3*], Wenqi Zhu[1, 2], Ting Xu[4*], Jay K. Lee[3], Henri J. Lezec[1] and Amit Agrawal[1, 2*]

[1]Center for Nanoscale Science and Technology, National Institute of Standards and Technology, Gaithersburg, MD 20899 USA

[2]Maryland NanoCenter, University of Maryland, College Park, MD 20742 USA

[3]Department of Electrical Engineering and Computer Science, Syracuse University, Syracuse, NY 13244 USA

[4]National Laboratory of Solid State Microstructures, College of Engineering and Applied Sciences, and Collaborative Innovation Center of Advanced Microstructures, Nanjing University, Nanjing 210093, China

Corresponding*: matthew.davis@nist.gov (M.S.D); xuting@nju.edu.cn (T. X.); amit.agrawal@nist.gov (A.A.)

Exploiting the wave-nature of light in its simplest form, periodic architectures have enabled a panoply of tunable optical devices with the ability to perform useful functions such as filtering, spectroscopy and multiplexing. Here, we remove the constraint of structural periodicity to enhance, simultaneously, the performance and functionality of passive plasmonic devices operating at optical frequencies. By using a physically-intuitive, first-order interference model of plasmon-light interactions, we demonstrate a simple and efficient route towards designing devices with flexible, multi-spectral optical response, fundamentally not achievable using periodic architectures. Leveraging this approach, we experimentally implement ultra-compact directional light-filters and colour-sorters exhibiting angle- or spectrally-tunable optical responses with high contrast, and low spectral or spatial crosstalk. Expanding the potential of aperiodic systems to implement tailored spectral and angular responses, these results hint at promising applications in solar-energy harvesting, optical signal multiplexing and integrated sensing.

INTRODUCTION

Scattering and interference phenomena govern the novel, and sometimes unexpected, physics associated with aperiodic optical systems that include weakly disordered, deterministic aperiodic, quasiperiodic and random structures [1-5]. While the underlying mechanisms governing localization and wave-transport in these devices require further elucidation, remarkable progress has occurred in areas such as random lasing and imaging [6-8]. In recent years, plasmonic systems, utilizing electromagnetic waves that are confined to a metal-dielectric interface, have allowed confinement and manipulation of light on length scales that are simply not possible with purely dielectric systems [9-12]. For example, periodic arrays of metallic and metallo-dielectric scatterers patterned on a deep-subwavelength scale, commonly referred to as metasurfaces, have demonstrated abrupt changes to the phase-front of light allowing complex wavefront shaping using flat-optical components of nanoscale thickness [13, 14]. One class of such structures, a periodic array of nanoscale apertures, slits or slit and grooves patterned on an opaque metal film, has shown promise as an efficient wavelength-scale transmission light-filter [15-17] and chemical/biological sensor [18-21]. The underlying periodicity inherent to these structures allows a wide-range of analytical methods to be used for device-design [22-25]. However, since periodicity a-priori limits the range of possible spectral responses, devices based on periodic structures are intrinsically limited in their functional characteristics. In comparison, aperiodic structures are less constrained in their configuration both in real and reciprocal space, and therefore potentially allow greater engineering control over the optical response of devices which incorporate them [26, 27]. A large variety of recently demonstrated aperiodic structures have added significant flexibility and richness towards engineering an optical response in ways not possible with periodic counterparts. For example, computationally intensive nonlinear search algorithms were employed to design ultra-compact polarization beam splitters and wavelength demultiplexers at telecom wavelengths, wherein the algorithm searched the full design-space of the device area with arbitrary topologies for the optimum solution [28, 29]. Alternate approaches utilizing the transfer matrix method [30], aperiodic Fourier modal method [31, 32] and field-

decomposition [33], or using asymmetric device profiles [34] have recently been used to predict the scattering properties of surface plasmon polaritons (SPPs) from subwavelength patterns on a metal surface, and were utilized to achieve dichroic beam splitting [35] and directional launching of SPPs for normally incident light at a single wavelength of interest [34, 36, 37]. However, the widespread use of aperiodic structures in optical devices has been inhibited to date by the constraints of computationally-intensive optimization based on multi-dimensional parameter searches using full electromagnetic numerical simulations [28, 29, 38].

Here, we show how the use of a physically-intuitive, first-order interference model of plasmon-light interactions enables straightforward design of aperiodic plasmonic devices with flexible and angle-dependent multi-spectral transmission signatures. Following this approach, we experimentally implement visible frequency transmission filters that leverage an aperiodic arrangement of metallic surface grooves to yield unique spectral and angular responses, in which a discrete set of input (or output) angles is mapped one-to-one to a discrete set of output (or input) frequencies. The device consists of a single-subwavelength linear slit (circular aperture) surrounded by multiple linear (annular) grooves on an opaque metal film with the position, width and depth of the grooves individually optimized to achieve the desired multi-spectral response at specific incident angles. The structure is designed using a nested-iterative search algorithm based on a physically intuitive first-order analytic model of interference, at the slit, between directly incident light and SPPs arriving from the illuminated grooves, each acting as SPP launch sites. Use of an aperiodic arrangement for groove placement with respect to the slit affords utmost flexibility in tailoring the spectral response of the device at arbitrary angles of incidence and over a broad spectral range simultaneously. The interference model is physically intuitive and vastly simplified compared to full numerical simulations typically underlying nonlinear search algorithms because it requires only knowledge of SPP coupling and phase-shift coefficients for optimum structure design. The deployment here of a first-order analytical model as the core of a numerical optimization algorithm serves to confirm that the fundamental interference mechanisms, shown to govern operation of periodic slit-

groove devices implemented to date, can also be successfully applied to the more general case of aperiodic plasmonic systems provided that other geometrical degrees of freedom are also enabled. This approach, involving only adjustment of in-plane dimensions (individual groove spacing and width), results in an easy-to-fabricate device having a complex multi-functional response at optical frequencies. Furthermore, we demonstrate that the model is broadly applicable by utilizing it to minimize the transmission spectral linewidth for a refractive index sensing application. Expanding the potential of aperiodic systems to implement tailored optical responses, these results hint at potential applications in hyperspectral imaging, multi-junction photovoltaics and integrated sensing.

RESULTS

First-order interference model for SPP-light interactions:

The spectral transmission response of an SPP-based slit-groove device can be explained by first analyzing the angle-dependent transmission through an interferometer consisting of an opaque metal film, facing a dielectric medium of refractive index n, and decorated with both a subwavelength-width through-slit (width: W) and a parallel subwavelength-width groove (width: w; depth: t) placed to the left of the slit at a centre-to-centre distance d (Figure 1a). The film is illuminated on the groove side, at an angle θ with respect to the surface normal, by a TM polarized plane-wave (free-space wavelength: λ_0; wavevector magnitude: k_0), with H-field parallel to the slit. H_0 designates the complex H-field amplitude of the incident wave at the slit; the corresponding H-field amplitude of the incident wave at the groove is then $H_0 e^{i\phi}$, where $\phi = -nk_0 d \sin\theta$ is the phase retardation of the plane-wave at the groove with respect to the slit. The incident light at the groove diffracts into an SPP mode of field amplitude $H_0 e^{i\phi}\beta e^{i\varphi}$, and mode index $n_{\mathrm{SPP}} + i\kappa_{\mathrm{SPP}}$, where real coefficients $\beta(w, t, \theta, \lambda_0)$ and $\varphi(w, t, \theta, \lambda_0)$ represent the amplitude and phase of the free-space (FS) to SPP coupling process (assumed to depend on groove width and depth as well as wavelength and angle of the incident light). The SPP propagates towards the slit, where it

arrives with complex field amplitude $H_0 e^{i\phi}\beta e^{i\varphi} e^{i\psi} e^{-(d/\alpha)}$, where $\psi = n_{\mathrm{SPP}} k_0 d$ and $\alpha = 1/(\kappa_{\mathrm{SPP}} k_0)$ are, respectively, the accumulated propagation phase and amplitude decay-length of the SPP along the surface. Finally, free-space and SPP modes incident upon the slit are converted into coherently superimposed guided modes inside the slit, with amplitude coupling coefficient $B(W, \theta, \lambda_0)$ and phase shift $\Phi(W, \theta, \lambda_0)$ for the plane wave incident upon the slit from free-space (where coupling is assumed to depend on slit width as well as both wavelength and incident angle), and coupling coefficient $B'(W, \lambda_0)$ and phase-shift $\Phi'(W, \lambda_0)$ for the SPP incident upon the slit along the metal interface (where coupling is assumed to depend only on the slit width and free-space wavelength). The net complex field amplitude at the output plane of the slit is then given by $H_{\mathrm{SG}} = T\left(H_0 B e^{i\Phi} + H_0 e^{i\phi}\beta\, e^{i\varphi} e^{i\psi} e^{-(d/\alpha)} B' e^{i\Phi'}\right)$, where T is the complex amplitude transmission coefficient of the slit. For reference, the complex field amplitude at the output plane of an isolated slit, illuminated under identical conditions, is given by $H_{\mathrm{S}} = T H_0 B e^{i\Phi}$. The groove-slit interference process then yields a net complex field amplitude at the output plane of the groove-decorated slit, relative to that of an isolated slit, given by

$$\gamma = \frac{H_{\mathrm{SG}}}{H_{\mathrm{S}}} = 1 + B_{\mathrm{eff}} e^{i\Phi_{\mathrm{eff}}} \beta e^{-(d/\alpha)} e^{i(\varphi+\psi-\phi)}, \quad (1)$$

where quantities $B_{\mathrm{eff}}(W, \theta, \lambda_0) = B'(W, \lambda_0)/B(W, \theta, \lambda_0)$ and $\Phi_{\mathrm{eff}}(W, \theta, \lambda_0) = \Phi'(W, \lambda_0) - \Phi(W, \theta, \lambda_0)$ represent, respectively, the amplitude and phase of the SPP-to-slit in-coupling process normalized to the amplitude and phase of the FS-to-slit in-coupling process. The corresponding transmitted intensity into the far-field for the slit-groove device, relative to that of an isolated slit, is then given by $\Gamma = |\gamma|^2$. The values of β and φ are calculated, in the case of a single slit-groove pair device patterned in a 250-nm-thick Ag film facing free-space, by curve-fitting the analytical expression for relative transmission intensity, Γ, to its value derived from two-dimensional finite-difference-time-domain (FDTD) simulations. The variations in β and φ as a function of both groove-width (w: 50 nm to 400 nm) and free-space wavelength (λ_0: 450 nm to 750 nm) for illumination at normal incidence ($\theta = 0°$) and fixed groove-depth ($t = 100$ nm) are shown in Figures 1b and 1c, respectively. The corresponding plots

for the variations in β and φ as a function of w and λ_0 for respective incident angles $\theta = 10°$ and $20°$ can be found in Supplementary Figure 1. The variations in B_{eff} and Φ_{eff} as a function of free-space wavelength (λ_0: 450 nm to 750 nm), for illumination angles of $\theta = 0°$, $10°$ and $20°$ and fixed slit-width ($W = 100$ nm) along with those in constituent parameters B, B', Φ and Φ' are shown in Supplementary Figure 2. Contributions from higher-order interference effects (such as multiple reflections of SPPs between the slit and the groove, or between grooves) are not taken into account as they are expected to be minimal [39].

This approach can now be extended to model the transmission characteristics of a device consisting of N grooves located to the left of a single slit, each having arbitrary depth and width (Figure 1d). Once again, the film is illuminated, at an angle θ with respect to the surface normal, with complex H-field amplitude H_0 at the slit. The corresponding H-field amplitude of the incident wave at the groove g_i (located at a distance d_i from the slit) is then $H_0 e^{i\phi_i}$, where $\phi_i = -nk_0 d_i \sin\theta$ is the phase retardation of the plane-wave at the groove with respect to the slit. Free-space illumination of the groove results in launching of an SPP mode towards the slit with relative amplitude and phase β_i and φ_i, respectively. Upon crossing any intermediate groove, g_j on its way to the slit, the SPP is modeled to undergo a phase-shift φ_j' and an amplitude reduction (modulation factor β_j') due to its interaction with that specific groove. In addition, the SPP experiences an accumulated propagation phase and amplitude decay length along the surface of $\psi_i = n_{\text{SPP}} k_0 d_i$ and α, respectively. Upon arrival at the slit entrance, this SPP couples to the slit with amplitude coupling coefficient $B'(W, \lambda_0)$ and phase-shift $\Phi'(W, \lambda_0)$, and coherently interferes with the waveguide modes resulting, from SPPs arriving from all the other grooves (and coupled into the slit with the same coupling coefficient and phase shift) and from direct illumination of the slit, with amplitude coupling coefficient $B(W, \theta, \lambda_0)$ and phase shift $\Phi(W, \theta, \lambda_0)$. The net normalized H-field transmission amplitude relative to that of an isolated slit then given by

$$\gamma_N = 1 + B_{\text{eff}} e^{i\Phi_{\text{eff}}} \sum_{i=1}^{N} \left(\beta_i e^{-(d_i/\alpha)} e^{i(\varphi_i + \psi_i - \phi_i)} \left(\prod_{j=1}^{i-1} \beta_j' e^{i\varphi_j'} \right)_{i>1} \right). \quad (2)$$

Generalizing the device to an aperiodic slit-groove structure having N grooves to the left and M grooves to the right of the slit, yields a normalized H-field transmission amplitude relative to that of an isolated slit of

$$\gamma_{MN} = \gamma_N + B_{\text{eff}} e^{i\Phi_{\text{eff}}} \sum_{i=1}^{M} \left(\beta_i e^{-(d_i/\alpha)} e^{i(\varphi_i + \psi_i + \phi_i)} \left(\prod_{j=1}^{i-1} \beta_j' e^{i\varphi_j'} \right)_{i>1} \right). \quad (3)$$

The corresponding relative transmission intensity into the far field is given by $\Gamma = |\gamma_{MN}|^2$. FDTD simulations of a slit-groove device having two grooves ($N = 2$, $M = 0$) are used to derive the dependence groove-crossing amplitude-drop β' and phase-slip φ' on groove-profile and illumination wavelength. The variations in β' and φ' as a function of both groove-width (w: 50 nm to 400 nm) and free-space wavelength (λ_0: 450 nm to 750 nm), at fixed groove-depth ($t = 100$ nm), are shown in Figures 1e and 1f, respectively. The first-order interference model of equation (3) forms the core of a multi-dimensional iterative optimization algorithm described as follows. Based on specifications for the model output, corresponding to desired characteristics for the transmitted intensity (such as spectral shape including discrete peak positions and linewidths), for given model inputs, corresponding to imposed illumination conditions (such as a range of free-space wavelengths and angles of incidence), the algorithm performs a nested iterative-adaptive search in which the number of grooves and individual position, width and depth of each groove are simultaneously varied, using a least-square criterion to establish convergence.

Aperiodic angle-selective colour filter:

The algorithm described above provides an elegant platform for engineering the optical response of aperiodic slit-groove transmission devices, and suggests a broader range of applications than is possible with periodic arrays. For example, while interference filters and waveplates provide an easy route towards

achieving high-contrast frequency and polarization selectivity, implementing optical frequency components that provide angular or directional selectivity over a broad spectral range represents a major technological challenge. Approaches utilizing anisotropic metamaterials and plasmonic slit-arrays have been proposed to achieve broadband angular selectivity, though at microwave frequencies [40, 41]. A one-dimensional photonic crystal was recently used to achieve complete transparency over a broad spectral range at one incident angle [42]. Here, we first use the algorithm to design a plasmonic angularly-selective colour filter that exhibits directionally modulated spectral output at optical frequencies under white-light plane-wave illumination. This filter yields tailored narrowband transmission spectra for specific incidence angles, where each spectral peak position (respectively in the red, green and blue) of the transmitted light corresponds to one of three pre-defined incident angles (Figure 2a). As an illustrative example, we target a structure that transmits light at centre wavelengths of 690 nm, 550 nm and 460 nm respectively, for incident angles of 0°, 10° and 20°, respectively. Based on the above spectral excitation and angular transmission specifications, along with the respective design choices of: (a) Ag as the constituent metal film, (b) five grooves to each side of the slit (*i.e.* $N = 5$ and $M = 5$, limiting the device-footprint to a lateral dimension of $L \leq 10$ μm), and (c) a fixed groove-depth $t = 100$ nm, the search algorithm is yields an optimized width and position for each groove relative to the slit. A schematic cross-section of the resulting aperiodic surface profile is shown in Figure 2b. The model-calculated transmission spectra for the slit-groove structure relative to that of an isolated slit, Γ (Figure 2c, solid lines), display a distinct spectral peak at each of the specified incidence angles (with red, blue and green peak positions of 670 nm, 545 nm and 476 nm, closely matching the respective target values). Each peak is characterized by low spectral crosstalk with respect to the two other peaks, as enforced by the search algorithm. The corresponding relative transmission spectra numerically-simulated using the FDTD technique (Figure 2c, dashed lines), where Ag-film thickness $h = 250$ nm and slit-width $W = 100$ nm are assumed, show remarkable agreement with the model spectra, validating in particular the efficacy of the assumptions underlying the first-order analytical model. The spectral peak locations resulting from the final aperiodic device design are also consistent with the associated spatial-frequency content denoted by

discrete peaks in the reciprocal-space representation of the projection of the surface profile onto the plane of incidence, for each of the three angles of incidence (Supplementary Figure 3). Aperiodic systems achieved using this approach differ from deterministic aperiodic geometries generated using substitution rules or self-similar inflation symmetries, and have been referred to as aperiodic systems by design in the literature [4, 43-45].

To further validate the efficacy of the aperiodic design, equivalent slit-groove devices where the grooves were arranged periodically or in a chirped (linear and exponential) geometry were designed for comparison (using constant groove width: $w = 50$ nm and groove depth: $t = 50$ nm). As a basis for comparison with the aperiodic design, the periodic and chirped devices were designed to also exhibit a spectral peak in transmission at 690 nm under normal incidence illumination (Supplementary Figure 4). For the other incidence angles of operation ($\theta = 10°$ and $20°$), however, correct spectral positioning of the targeted transmission peaks was not possible: the chirped devices exhibit a complex transmission spectra with no specific trend, whereas the spectral peak in the periodic device shifts to shorter wavelengths that are determined by its spatial-frequency content (Supplementary Figure 5). This comparison clearly illustrates that the underlying periodicity a-priori determines the spectral (or spatial) response of devices based on periodic architectures, and hence these devices cannot achieve the flexibility in engineering the optical response possible with aperiodic systems by design. Finally, random placement of the above grooves within the 10 μm-wide lateral footprint of the device yields a total absence of angular-spectral control, as evidenced by the transmission spectrum of one such random device (Supplementary Figure 4d).

The groove profile yielded by the optimization algorithm (Figure 2b) was experimentally implemented (Figure 2d) into a Ag-film on an indium-tin-oxide (ITO) coated fused-silica substrate. The groove structure was defined using a sequential combination of electron-beam lithography and lift-off of an initial Ag-film (100-nm-thick), followed by further evaporation of another Ag-film (150-nm-thick). Focused-ion-beam (FIB) milling was then used to define a 100-nm-wide, 10-μm-long through slit

(Methods, and Supplementary Figure 6 for fabrication details). A reference device consisting of an isolated 100-nm-wide through slit on the same Ag-film was also fabricated by FIB milling. The spectral transmission characteristics of the device were measured by illuminating it with a TM-polarized supercontinuum white light laser at three angles of incidence (0°, 10° and 20°) with respect to the surface normal, with H-field parallel to the slit-length. The light transmitted through the device was collected using a 100× microscope objective (numerical aperture, NA = 0.75) and directed to a grating spectrometer coupled to a charge-coupled device (CCD) camera. The experimentally measured relative transmission spectra at each angle of incidence (normalized to that of the isolated reference slit) are shown in Figure 2e. A close match to the model predictions were obtained, namely: distinct red, green and blue spectral peaks, respectively, at each of the illumination angles; peak positions of 690 nm, 545 nm and 480 nm, closely matching both target and analytic model-computed values; and low-crosstalk evidenced by low-transmittance out-of-band spectral features that match the analytic predictions. Non-optimized, full-width-at-half-maximum ($\Delta\lambda_{1/2}$) linewidth values for each of the peaks are 60 nm ($\theta = 0°$), 60 nm ($\theta = 10°$) and 38 nm ($\theta = 20°$), respectively, which are systematically smaller by a factor of approximately two to four compared to those reported in the literature for plasmonic transmission devices incorporating periodic arrays of grooves [46-48]. The optical contrast, linewidth and spectral crosstalk performance of the optimized angle-resolved colour sorter is further discussed in Supplementary Note 1 and Supplementary Tables 1 and 2. Moreover, mapping the angle of incident radiation to a given colour using optimized aperiodic groove positions can be readily extended to more than three input angles (e. g., five as shown in Supplementary Figure 7). The complete summary of the aperiodic device implementation procedure including modeling and optimization, nanofabrication and experimental characterization is outlined in Supplementary Figure 8. Note that the absolute transmission efficiency of the aperiodic device at the spectral peak locations is on the order of 1.5 % to 3 % across the visible frequency range for illumination with a TM polarized light. For reference, the FDTD-simulated absolute transmission efficiency of an isolated single-slit as a function of Ag-film thickness h and slit-width W, for

a normally incident TM polarized light at three wavelengths (690 nm, 550 nm, and 460 nm) is shown in Supplementary Figure 9.

Anti-symmetric Spatial Spectrum Splitting:

Spectrum splitting using diffractive optics has been utilized in recent years to enhance the photovoltaic output power in solar cells [49] as well as for hyperspectral imaging applications [15, 46, 50]. Periodic plasmonic antennas have also been utilized to achieve symmetric, angularly-continuous, directional spectral sorting of white-light [47] or emission from quantum dots and fluorophores [51, 52]. The angle-resolved colour sorter described above, on the other hand, can be exploited to achieve anti-symmetric spatial spectrum-splitting, in other words, spectrally resolving transmitted light into different angles all belonging to a single angular half-space with respect to the normal. This functionality results upon illumination of the un-patterned side of the structure with white-light, *i.e.* "reverse illumination", leading to emergence of a discrete set of colour-sorted beams from the patterned side, each traveling along a different, pre-defined angle to one side of the normal only (Figure 3, top panel). For experimental characterization of this effect, the fabricated device was illuminated at normal incidence on its groove-free side using a TM-polarized supercontinuum white light laser light with H-field parallel to the slit-length (oriented along the y-direction at $x = 0$, Figure 3). The colour and intensity distribution of the transmitted light in a far-field plane located at a distance $\Delta z = 17.5$ μm from the device exit surface was imaged using an inverted optical microscope (100×, NA = 0.75 microscope objective) and a colour-CCD camera (where the x-position of the transmitted light field relative to the centre of the slit is calibrated by imaging the exit surface of a reference single-slit illuminated under identical conditions). By directly measuring the distance of the local intensity maximum of the red, green and blue streaks relative to the centre of the slit, Δx, the diffraction angles for the red, blue and green light are determined to be 0° ± 0.49°, 9.72° ± 0.47°, and 18.92° ± 0.44° respectively. The uncertainty in measurement of angles is one standard deviation, and calculated from the uncertainty in measuring the distances of the red, green and

blue streaks relative to the normal to the slit due to the finite pixel-spacing of the CCD camera. The measured angles are close to the angles specified for angle-selective colour-filter operation under "forward illumination" (0°, 10° and 20° respectively), verifying the time-reversal symmetric behavior expected for any linear device. Note that the same spectrally resolved angular output response can be achieved for any angle of "reverse illumination" on the un-patterned side, the slit acting as a spatial filter. This approach to map the wavelength of incident radiation to a given angle can also be readily extended to more than three input wavelengths (*e.g.* five, by applying reciprocity to the result of Supplementary Figure 7) allowing hyperspectral imaging where a spectral image cube can be directly acquired in a single exposure using a two-dimensional array of such devices coupled to an imaging chip. In contrast to other spectral imaging techniques, the colour-sorting approach presented here does not rely on filters or scanning interferometers that require long acquisition times for spectral-cube measurements. The multi-colour functionality achieved here with a single-device stands in contrast to the mono-colour functionality, characteristic of periodic plasmonic structures that require physically separate structures to achieve a full set of discrete colour responses [16, 17, 46, 53, 54].

Bullseye directional light filter:

Angle-selective colour filtering can also be realized by replacing an input surface decorated with an aperiodic collection of linear grooves surrounding a linear subwavelength-width slit, with one decorated with an aperiodic collection of circular concentric grooves surrounding a circular subwavelength-diameter aperture, forming an aperiodic bullseye pattern (Figure 4a). Such a structure offers an additional rotational degree of freedom in obtaining different output spectra under white-light illumination for a given collection of input angles for a fixed plane of incidence and fixed TM polarization with respect to the surface (H-field vector in the plane of the bullseye). This is achieved by dividing up the bullseye into a discrete number of angular sectors (Figure 4a, showing two such sectors), each having a distinct aperiodic groove arrangement. Each angular sector can then be individually addressed for a unique target colour

response as a function of polar angle, θ, with respect to the principle axis of the aperture, by rotating the bullseye about that axis to an azimuthal angle, ϕ, such that the direction of the H-field vector is azimuthally centred within that sector. To implement such a ϕ addressable, azimuthal angle-selective colour-filter, a bullseye with two different functional sectors was designed using the optimization algorithm incorporating the one-dimensional interference model of equation (3), treating the curved grooves in a manner equivalent to the linear grooves. The device targets three specific illumination angles for colour sorting into two staggered sets of output wavelengths in the visible (listed in Supplementary Table 3) for $\phi = 0°$ and 90°, respectively. The model-calculated transmission spectra relative to that of an isolated circular aperture, Γ, for a bullseye structure consisting of two distinct aperiodic angular sectors, arranged orthogonally at $\phi = 0°$ and 90°, and probed at three different polar angles of incidence ($\theta = 0°,\ 10°$ and $20°$) show a distinct spectral peak, one for each of the six unique illumination conditions (Figures 4b and 4c, solid lines), closely matching the target values (Supplementary Table 3). The corresponding relative transmission spectra numerically-simulated using the FDTD technique (Figures 4b and 4c, dashed lines), where Ag-film thickness $h = 250$ nm and aperture-diameter $d_0 = 100$ nm are assumed, show remarkable agreement with the model generated spectra. The aperiodic-bullseye was experimentally implemented (Figure 4d) on an ITO coated fused-silica substrate using the same fabrication sequence as the linear slit-groove device (Methods, and Supplementary Figure 6). A reference device consisting of an isolated aperture of identical dimensions through the same Ag-film was also fabricated by FIB milling. The spectral transmission characteristics of the device, at its two azimuth orientations ($\phi = 0°$ and $90°$), was measured by illuminating it with a TM-polarized supercontinuum white light laser (H-field vector in the plane of the bullseye) at three angles of incidence ($\theta = 0°$, $10°$ and $20°$) for a fixed plane of incidence. The experimentally measured relative transmission spectra at each angle of incidence (normalized to that of the isolated reference aperture) are shown in Figures 4e and 4f. A close match to the model predictions are obtained: namely, six distinct spectral peaks at each of the illumination conditions, and peak positions closely matching both target and analytic model-computed

values (Supplementary Table 3). The multi-spectral response of the aperiodic bullseye structure wherein a particular spectrum is directly related to a specific directionality of the incident beam (θ) and rotational orientation of the device (ϕ) suggests applications as a directional light sensor in three-dimensions.

Narrow linewidth refractive index sensing:

The aperiodic colour filters designed in this study are limited to five grooves each on both sides of the central slit within a lateral device footprint of approximately 10 μm, and the structural parameters of each groove was optimized to achieve angular colour selectivity at multiple angles of incidence simultaneously. However, for alternate applications such as refractive-index sensing, it is straightforward to redefine the angular and spectral target constraints input to the optimization algorithm to instead perform linewidth optimization (at the cost of angular selectivity) for a single angle of incidence within the same device-footprint. Spectral linewidth is inversely related to the figure-of-merit (FOM), which is a metric used to compare the performance of refractive index optical sensors, and is defined as: FOM $= S_{\mathrm{b}}/\Delta\lambda_{1/2}$, where $S_{\mathrm{b}} = \Delta\lambda/\Delta n$ is the bulk index-sensitivity of the device, $\Delta\lambda$ is the spectral peak shift for a change Δn of the refractive index of the surrounding media, and $\Delta\lambda_{1/2}$ is the full-width at half-maximum (FWHM) linewidth of the spectral peak [55]. Here, we experimentally implement an aperiodic linear slit-groove Ag structure for which white-light illumination of the groove-decorated side at normal incidence yields narrow linewidth transmission at a centre wavelength of 540 nm. The optimization algorithm yields an aperiodic device configuration for which the modeled transmission spectrum under illumination at $\theta =$ 0° exhibits a distinct peak at a centre-wavelength of 540 nm characterized by narrow linewidth $\Delta\lambda_{1/2} \approx$ 14.1 nm (Figure 5a, dashed line). The corresponding relative transmission spectra numerically-simulated using the FDTD technique (Figure 5a, solid line), where Ag-film thickness $h =$ 250 nm and slit-width $W =$ 100 nm are assumed, show remarkable agreement with the model generated spectra. The aperiodic sensing device was experimentally implemented (Figure 5b) on an ITO coated fused-silica substrate using the same fabrication sequence as the other aperiodic devices (Methods, and Supplementary Figure 6). To

evaluate the performance of a refractive-index sensor based on the aperiodic slit-groove array, we expose the Ag-air interface to a superficial perturbation in index of refraction under the form of ultra-thin Al_2O_3 layers of index n = 1.77 of thickness ranging from 1 nm to 9 nm (Figure 5c), conformally deposited using atomic layer deposition. Nanometer-scale spectral shifts of the spectral peak to longer wavelengths, as a function of increasing layer thickness (Figures 5c and 5d), are easily resolvable due to the narrow resonance linewidth characteristic of the device. The experiments yield a refractive index wavelength sensitivity $S_{\mathrm{b}} = \Delta\lambda/\Delta n \approx 330$ nm·RIU^{-1}, along with an FOM $= S_{\mathrm{b}}/\Delta\lambda_{1/2} \approx 22.3$ that is comparable to that of a state-of-the-art, commercial SPR sensor based on Kretschmann configuration excitation [56] as well as plasmonic interferometric sensors [57]. The effective refractive index change (Δn) is determined using an effective medium approximation of dielectric bi-layer coating the metal surface into a single dielectric medium of refractive index n_{eff} (Supplementary Note 2). Finally, the applicability of multi-band spectral transmission of the aperiodic devices for multiplexed plasmon sensing applications is demonstrated for five spectral peaks spanning the visible frequency range (Supplementary Note 3).

DISCUSSION

The performance (in terms of spectral or spatial crosstalk, and sensing FOM) of the aperiodic devices studied here is primarily limited by the losses in the as-deposited evaporated Ag-film, wherein the 1/e SPP decay length (L_{SPP}) placed an upper-limit on the lateral footprint of the device to $L \leq 10$ μm. The experimentally measured value of L_{SPP} for the evaporated Ag-films used in the experiments, at a free-space wavelength of 690 nm, is determined to be $L_{\mathrm{SPP}} = 7$ μm (Supplementary Note 4). This limit on lateral device footprint was also determined from the dependence of spectral response of the aperiodic colour filter on the number of grooves wherein the spectral response saturated with increasing number of grooves (reaching saturation at $N = M = 5$, Supplementary Figure 13). However, based on recent progress in using the template-stripping approach to create ultra-smooth Ag films with typical values of L_{SPP} ranging from 30 μm to 80 μm [58, 59], utilizing template-stripped Ag-films would be one very

straightforward approach to enhance the performance of these devices. The template-stripping approach also directly lends itself towards fabricating the inverse groove structures onto reusable Si templates where groove-depth along with its width and location can be used as a free-parameter to further improve the flexibility in device-design. Finally, regarding the interference model, incorporating higher-order SPP-SPP and SPP-incident light interactions would allow for a more accurate prediction of the resonance lineshape and spectral peaks that closely match those predicted by numerical solvers or measured experimentally.

In conclusion, we have developed a robust interference-based first-order analytical model to calculate the transmission properties of plasmonic devices with aperiodic topologies. Incorporating the model into a structural optimization algorithm enables straightforward design of ultra-compact directional light-filters and colour-sorters exhibiting angle- or spectral-tunable optical responses with both high contrast and low spectral or spatial crosstalk, hinting at promising applications in solar-energy harvesting, optical signal multiplexing and high-figure-of-merit refractive index sensing. By substituting, as the core of the optimization process, an analytical physical model for brute-force numerical simulation, we demonstrate a simple and efficient route towards leveraging aperiodic topologies to achieve devices with flexible and multi-spectral optical functions that are fundamentally not achievable using periodic architectures.

METHODS

Fabrication

The aperiodic colour-filter structures are fabricated on 20-nm-thick ITO coated fused silica substrates. Electron-beam lithography at 100 keV was used to expose the inverse groove pattern on the 100-nm-thick poly-methyl methacrylate (PMMA) resist spun-coated on the substrates. After the exposure, PMMA was developed for 60 s in methyl isobutyl ketone (MIBK) followed by a 30 s rinse in isopropyl alcohol (IPA). Electron-beam evaporation was used to deposit a 5-nm-thick Cr adhesion layer, followed by a 100-nm-

thick Ag-film. A twelve-hour soak in acetone was used for lift-off leaving rectangular islands of Ag at the location of the exposed areas. A second Ag deposition of thickness 150 nm was performed using electron-beam evaporation in order to elevate the groove pattern by an optically thick layer above the plane of the substrate. Finally, focused-ion-beam milling was used to create a 100-nm-wide, 10-μm-long central through slits (or 150-nm-diameter circular through apertures). The fabrication steps are schematically outlined in Supplementary Figure 6. For the sensing device, the patterned Ag-air interface was conformally coated with an ultra-thin layer of Al_2O_3 of thickness ranging from 1 nm to 9 nm using atomic layer deposition.

Measurements

For experimental characterization, the samples were illuminated using a TM polarized supercontinuum white light laser (emission wavelength range: 400 nm to 2000 nm) at various angles of incidence, and sample orientation. The angle of incidence at the sample was controlled using a motorized rotation-tilt-mirror mounted on a linear translation stage. For spectral measurements, the light transmitted through the devices was collected using 100× microscope objective ($\mathrm{NA} = 0.75$) and directed to a grating spectrometer connected to a cooled Si-CCD camera. In each case, the transmitted intensity from the linear slit-groove (bullseye) device was normalized to that of an isolated reference slit (circular aperture). For spectral splitting experiments, accurate referencing of the focal plane of the optical microscope relative to the exit surface of the device was achieved by imaging the exit surface (Δz = 0 μm) of the device. The colour and intensity distribution of the transmitted light in a far-field plane located at a distance Δz = 17.5 μm from the device exit surface was imaged using an inverted optical microscope (100×, $NA = 0.75$ microscope objective) and a colour-CCD camera. The x-position of the transmitted light field relative to the centre of the slit was calibrated by imaging the exit surface of a reference single-slit illuminated under identical conditions. By directly measuring the distance of the local intensity maximum of the red, green

and blue streaks relative to the centre of the slit, Δx, the diffraction angles, $\theta = \tan^{-1}(\Delta x/\Delta z)$ for the red, blue and green light were determined.

DATA AVAILABILITY

All data needed to evaluate the conclusions in the paper are present in the paper and the Supplementary Information. Additional data available from the corresponding author upon reasonable request.

REFERENCES

[1] Segev, M., Silberberg, Y. and Christodoulides, D. N. Anderson localization of light. *Nature Photonics* **7**, 197–204 (2013).

[2] Wiersma, D. S. Disordered photonics. *Nature Photonics* **7**, 188–196 (2013).

[3] Vardeny, Z. V., Nahata, A. and Agrawal, A. Optics of photonic quasicrystals. *Nature Photonics* **7**, 177–187 (2013).

[4] Maciá, E. Exploiting aperiodic designs in nanophotonic devices. *Reports on Progress in Physics* **75**, 36502 (2012).

[5] Dal Negro, L. and Boriskina, S. V. Deterministic aperiodic nanostructures for photonics and plasmonics applications. *Laser & Photonics Reviews* **6**, 178–218 (2012).

[6] Mosk, A. P., Lagendijk, A., Lerosey, G. and Fink, M. Controlling waves in space and time for imaging and focusing in complex media. *Nature Photonics* **6**, 283–292 (2012).

[7] Bertolotti, J., van Putten, E. G., Blum, C., Lagendijk, A., Vos, W. L. and Mosk, A. P. Non-invasive imaging through opaque scattering layers. *Nature* **491**, 232–234 (2012).

[8] Wiersma, D. S. The physics and applications of random lasers. *Nature Physics* **4**, 359–367 (2008).

[9] Maier, S. A. *Plasmonics: Fundamentals and Applications*. (Springer US, 2007).

[10] Ozbay, E. Plasmonics: Merging photonics and electronics at nanoscale dimensions. *Science* **311**, 189–193 (2006).

[11] Gramotnev, D. K. and Bozhevolnyi, S. I. Plasmonics beyond the diffraction limit. *Nature Photonics* **4**, 83–91 (2010).

[12] Schuller, J. A., Barnard, E. S., Cai, W., Jun, Y. C., White, J. S. and Brongersma, M. L. Plasmonics for extreme light concentration and manipulation. *Nature Materials* **9**, 193–204 (2010).

[13] Yu, N. and Capasso, F. Flat optics with designer metasurfaces. *Nature Materials* **13**, 139–150 (2014).

[14] Minovich, A. E., Miroshnichenko, A. E., Bykov, A. Y., Murzina, T. V., Neshev, D. N. and Kivshar, Y. S. Functional and nonlinear optical metasurfaces. *Laser & Photonics Reviews* **9**, 195–213 (2015).

[15] Haïdar, R., Vincent, G. G., Collin, S. P., Bardou, N., Guérineau, N., Deschamps, J. L. and Pelouard, J. L. Free-standing subwavelength metallic gratings for snapshot multispectral imaging. *Applied Physics Letters* **96**, 221104 (2010).

[16] Yokogawa, S., Burgos, S. P. and Atwater, H. A. Plasmonic color filters for CMOS image sensor applications. *Nano Letters* **12**, 4349–4354 (2012).

[17] Xu, T., Wu, Y. K., Luo, X. and Guo, L. J. Plasmonic nanoresonators for high-resolution color filtering and spectral imaging. *Nature Communications* **1**, 59 (2010).

[18] Yanik, A. A., Huang, M., Kamohara, O., Artar, A., Geisbert, T. W., Connor, J. H. and Altug, H. An optofluidic nanoplasmonic biosensor for direct detection of live viruses from biological media. *Nano Letters* **10**, 4962–4969 (2010).

[19] Gordon, R., Sinton, D., Kavanagh, K. L. and Brolo, A. G., A new generation of sensors based on extraordinary optical transmission. *Acc. Chem. Res.* **41**, 1049–1057 (2008).

[20] Martín-Becerra, D., Armelles, G., González, M. U. and García-Martín, A. Plasmonic and magnetoplasmonic interferometry for sensing. *New Journal of Physics* **15**, 085021 (2013).

[21] Siu, V. S., Feng, J., Flanigan, P. W., Palmore, G. T. R. and Pacifici, D. A "plasmonic cuvette": dye chemistry coupled to plasmonic interferometry for glucose sensing. *Nanophotonics* **3**, 125–140 (2014).

[22] Garcia de Abajo, F. J. Light scattering by particle and hole arrays. *Reviews of Modern Physics* **79**, 1267–1290 (2007).

[23] Garcia-Vidal, F. J., Martin-Moreno, L., Ebbesen, T. W. and Kuipers, L. Light passing through subwavelength apertures. *Reviews of Modern Physics* **82**, 729–787 (2010).

[24] Martin-Moreno, L., Garcia-Vidal, F. J., Lezec, H. J., Pellerin, K. M., Thio, T., Pendry, J. B. and Ebbesen, T. W. Theory of extraordinary optical transmission through subwavelength hole arrays. *Physical Review Letters* **86**, 1114–1117 (2001).

[25] van Beijnum, F., Rétif, C., Smiet, C. B., Liu, H., Lalanne, P. and van Exter, M. P. Quasi-cylindrical wave contribution in experiments on extraordinary optical transmission. *Nature* **492**, 411–414 (2012).

[26] Matsui, T., Agrawal, A., Nahata, A. and Vardeny, Z. V. Transmission resonances through aperiodic arrays of subwavelength apertures. *Nature* **446**, 517–521 (2007).

[27] Pacifici, D., Lezec, H. J., Sweatlock, L. A., Walters, R. J. and Atwater, H. A. Universal optical transmission features in periodic and quasiperiodic hole arrays. *Optics Express* **16**, 9222–9238 (2008).

[28] Shen, B., Wang, P., Polson, R. C. and Menon, R. An integrated-nanophotonic polarization beamsplitter with 2.4 x 2.4 μm^2 footprint. *Nature Photonics* **9**, 378–382 (2015).

[29] Piggott, A. Y., Lu, J., Lagoudakis, K. G., Petykiewicz, J., Babinec, T. M. and Vučković, J. Inverse design and demonstration of a compact and broadband on-chip wavelength demultiplexer. *Nature Photonics* **9**, 374–377 (2015).

[30] Huang, X. and Brongersma, M. L. Rapid computation of light scattering from aperiodic plasmonic structures. *Physical Review B.* **84**, 245120 (2011).

[31] Liu, H., Lalanne, P., Yang, X. and Hugonin, J. P. Surface plasmon generation by subwavelength isolated objects. *IEEE Journal of Selected Topics in Quantum Electronics* **14**, 1522–1529 (2008).

[32] Liu, H. and Lalanne, P. Light scattering by metallic surfaces with subwavelength patterns. *Physical Review B* **82**, 115418 (2010).

[33] Li, G., Xiao, F., Cai, L., Alameh, K. and Xu, A. Theory of the scattering of light and surface plasmon polaritons by finite-size subwavelength metallic defects via field decomposition. *New Journal of Physics* **13**, 73045 (2011).

[34] Yao, W. *et al.* Efficient directional excitation of surface plasmons by a single-element nanoantenna. *Nano Letters* **15**, 3115–3121 (2015).

[35] Liu, J. S. Q., Pala, R. A., Afshinmanesh, F., Cai, W. & Brongersma, M. L. A submicron plasmonic dichroic splitter. *Nature Communications* **2**, 525 (2011).

[36] Huang, X. & Brongersma, M. L. Compact aperiodic metallic groove arrays for unidirectional launching of surface plasmons. *Nano Letters* **13,** 5420–5424 (2013).

[37] Li, K., Xiao, F., Lu, F., Alameh, K. & Xu, A. Unidirectional coupling of surface plasmons with ultra-broadband and wide-angle efficiency: potential applications in sensing. *New Journal of Physics* **15,** 113040 (2013).

[38] Wiecha, P. R. Arbouet, A., Girard, C., Lecestre, A., Larrieu, G. & Paillard, V. Evolutionary multi-objective optimization of colour pixels based on dielectric nanoantennas. *Nature Nanotechnology* **12**, 163–169 (2016).

[39] Pacifici, D., Lezec, H. J., Atwater, H. A. and Weiner, J. Quantitative determination of optical transmission through subwavelength slit arrays in Ag films: the essential role of surface wave interference and local coupling between adjacent slits. *Physical Review B.* **77**, 115411 (2008).

[40] Alù, A., D'Aguanno, G., Mattiucci, N. and Bloemer, M. J. Plasmonic Brewster angle: Broadband extraordinary transmission through optical gratings. *Physical Review Letters* 106, 123902 (2011).

[41] Aközbek, N., Mattiucci, N., de Ceglia, D., Trimm, R., Alù, A., D'Aguanno, G., Vincenti, M. A., Scalora, M. and Bloemer, M. J. Experimental demonstration of plasmonic Brewster angle

extraordinary transmission through extreme subwavelength slit arrays in the microwave. *Physical Review B* **85**, 205430 (2012).

[42] Shen, Y., Ye, D., Celanovic, I., Johnson, S. G., Joannopoulos, J. D. and Soljačić, M. Optical broadband angular selectivity. *Science* **343**, 1499–1501 (2014).

[43] Maciá, E. *Aperiodic Structures in Condensed Matter: Fundamentals and Applications*. (Taylor & Francis CRC, Boca Raton FL, USA 2009).

[44] Maciá, E. The importance of being aperiodic: Optical devices. In L. Dal Negro (Ed.), *Optics of Aperiodic Structures: Fundamentals and Device Applications* pp. 57-90. (Pan Stanford, USA 2014).

[45] Maciá, E. Thermal emission control via bandgap engineering in aperiodically designed nanophotonic devices. *Nanomaterials* **5**, 814–825 (2015).

[46] Laux, E., Genet, C., Skauli, T. and Ebbesen, T. W. Plasmonic photon sorters for spectral and polarimetric imaging. *Nature Photonics* **2**, 161–164 (2008).

[47] Lezec, H. J., Degiron, A., Devaux, E., Linke, R. A., Martin-Moreno, L., Garcia-Vidal, F. J. and Ebbesen, T. W. Beaming light from a subwavelength aperture. *Science* **297**, 820–822 (2002).

[48] Dunbar, L. A., Guillaumée, M., de León-Pérez, F., Santschi, C., Grenet, E., Eckert, R., López-Tejeira, F., García-Vidal, F. J., Martín-Moreno, L. and Stanley, R. P. Enhanced transmission from a single subwavelength slit aperture surrounded by grooves on a standard detector. *Applied Physics Letters* **95**, 011113 (2009).

[49] Kim, G., Dominguez-Cabellero, J. A., Lee, H., Friedman, D. J. and Menon, R., Increased photovoltaic power output via diffractive spectrum separation. *Physical Review Letters* **110**, 123901 (2013).

[50] Burgos, S. P., Yokogawa, S. and Atwater, H. A. Color imaging via nearest neighbor hole coupling in plasmonic color filters integrated onto a complementary metal-oxide semiconductor image sensor. *ACS Nano* **7**, 10038–10047 (2013).

[51] Aouani, H., Mahboub, O., Devaux, E., Rigneault, H., Ebbesen, T. W. and Wenger, J. Plasmonic antennas for directional sorting of fluorescence emission. *Nano Letters* **11**, 2400–2406 (2011).

[52] Jun, Y. C., Huang, K. C. Y. and Brongersma, M. L. Plasmonic beaming and active control over fluorescent emission. *Nature Communications* **2**, 283 (2011).

[53] Walls, K., Chen, Q., Grant, J., Collins, S., Cumming, D. R. S. and Drysdale, T. D. Narrowband multispectral filter set for visible band. *Optics Express* **20**, 21917–21923 (2012).

[54] Sounas, D. L. and Alù, A. Color separation through spectrally-selective optical funneling. *ACS Photonics* **3**, 620−626 (2016).

[55] Valsecchi, C. and Brolo, A. G. Periodic metallic nanostructures as plasmonic chemical sensors. *Langmuir* **29**, 5638–5649 (2013).

[56] Wang, X. -Y., Wang, Y. -L., Wang, S., Li, B., Zhang, X. -W., Dai, L. and Ma, R. -M. Lasing enhanced surface plasmon resonance sensing. *Nanophotonics* **5**, 52–58 (2016).

[57] Zeng, B., Gao, Y. & Bartoli, F. J. Differentiating surface and bulk interactions in nanoplasmonic interferometric sensor arrays. *Nanoscale* **7,** 166–170 (2015).

[58] McPeak, K. M., Jayanti, S. V., Kress, S. J., Meyer, S., Iotti, S., Rossinelli, A. and Norris, D. J. Plasmonic films can easily be better: rules and recipes. *ACS Photonics* **2**, 326–333 (2015).

[59] Zhu, W., Xu, T., Agrawal, A. and Lezec, H. J. Surface-Plasmon-Polariton laser based on an open-cavity Fabry-Perot resonator. Preprint at https://arxiv.org/abs/1610.03864 (2016).

Acknowledgements

M. S. D., W. Z., T. X. and A. A. acknowledge support under the Cooperative Research Agreement between the University of Maryland and the National Institute of Standards and Technology, Center for Nanoscale Science and Technology, Award#70NANB14H209, through the University of Maryland. T.X. acknowledges support from the Thousand Talents Program for Young Professionals, Collaborative Innovations Center of Advanced Microstructures and the Fundamental Research Funds for the Central Universities.

Author contributions

M. S. D. designed, fabricated and characterized the devices with assistance from W. Z., T. X. and A. A. J. K. L., H. J. L. and A. A. directed the project. All authors contributed to the interpretation of results and participated in manuscript preparation.

Additional information

Supplementary Information accompanies this paper at doi:

Competing interests: The authors declare no competing financial interests.

Figure Captions

Figure 1 | Transmission mechanism through an aperiodic slit-groove device. a, H-field amplitude transmission from a slit in the presence of a single-groove placed to its left, illuminated by a TM polarized white light laser (H-field parallel to the slit-length) at an angle θ on a metal-dielectric interface, where d is the distance between the slit and the groove (of width w and depth t). The SPP coupling process at the location of the groove is characterized by a real coupling coefficient β and phase φ. **b and c,** Variation in β and φ as a function of both groove-width (w: 50 nm to 400 nm) and free-space wavelength (λ_0: 450 nm to 750 nm), for illumination at normal incidence ($\theta = 0°$) and fixed groove-depth ($t = 100$ nm) at a Ag-air interface. **d,** H-field amplitude transmission through a device consisting of N grooves located to the left of an isolated slit. The propagation of an SPP coupled from an arbitrary groove g_N propagating over an intermediate groove on its way to the slit undergoes a phase-shift φ' and an amplitude reduction of a factor β'. In both **a** and **d**, the superimposed guided-mode propagation, through the slit, of both the free-space light and the SPP is characterized by a relative H-field coupling coefficient B_{eff} and phase-shift Φ_{eff} (Supplementary Figure 2). **e and f,** Variation in β' and φ' as a function of groove-width (w: 50 nm to 400 nm) of an intermediate groove, and free-space wavelength (λ_0: 450 nm to 750 nm), and fixed groove-depth ($t = 100$ nm) at a Ag-air interface.

Figure 2 | Aperiodic directional RGB colour-filter. a, Schematic illustration of the angle-dependent light transmission characteristics of an angularly-selective aperiodic RGB colour filter. The device is targeted to transmit red light at an incidence angle $\theta = 0°$, green at $\theta = 10°$, and blue at $\theta = 20°$ when illuminated with a TM polarized white-light laser source. The device consists of a subwavelength-width linear slit surrounded by five-grooves each on both sides within a total lateral device dimension of ≤ 10 μm. **b,** Model predicted surface cross-section profile of the optimized device at a Ag-air interface. Scale bar represents 1 μm. **c,** Relative transmission (Γ) spectra calculated using the interference model of equation (3) (solid lines) and FDTD simulations (dashed lines) show remarkable agreement, and demonstrate the unique spectral transmission characteristics of the device. **d,** Scanning-electron-microscope image of the patterned surface of the aperiodic slit-groove array device taken at 38° from the surface normal. The device is fabricated using the procedure described in Methods and outlined in Supplementary Figure 6. Horizontal scale bar represents 2 μm. **e,** Experimentally measured Γ spectra at three angles of incidence for the fabricated device. The spectral characteristics of the fabricated device, namely: linewidth, optical contrast and spectral cross-talk, are summarized in Supplementary Tables 1 and 2.

Figure 3 | Spectrum-splitting using the aperiodic slit-groove device. top panel, Schematic illustration of the device transmission under "reverse illumination" from the non-patterned side. Owing to reciprocity, the device when illuminated with TM polarized white light laser source from the non-patterned side is able to spatially separate the three-colours along well-defined discrete angles on the same side of the surface normal. **bottom panel,** Wide-field projected image of the transmitted light, collected at a distance $\Delta z = 17.5$ μm from the exit-surface of the device, using an inverted optical microscope (100×, NA = 0.75 microscope objective) connected to a colour-CCD camera. Scale bar along the *x*-axis in the CCD image represents 6.5 μm. The diffraction angle $\theta = \tan^{-1}(\Delta x/\Delta z)$ for the three colours is determined by directly measuring the distance of the local intensity maximum of the red, green and blue streaks relative to the centre of the slit, Δx. The experimentally measured diffraction angles for the red, green and blue colours (0° ± 0.49°, 9.72° ± 0.47° and 18.92° ± 0.44°, respectively) match closely the angles specified for angle-selective colour-filter operation under "forward illumination" (0°, 10° and 20°, respectively).

Figure 4 | Aperiodic bullseye directional light-filter. a, Schematic illustration of the light-transmission through an aperiodic bullseye structure consisting of two distinct radially integrated linear aperiodic slit-groove structures. **b** and **c,** Relative transmission (Γ) spectra calculated using the interference model of equation (3) (solid lines) and FDTD simulations (dashed lines) for $\theta = 0°$, 10° and 20° at both $\phi = 0°$ (**b**) and 90° (**c**). The calculated and simulated spectra agree with each other and demonstrate the incident angle (θ) and sample orientation (ϕ) dependent multi-spectral response of the device. **d,** Top-down scanning-electron-microscope image of the bullseye device fabricated following the same procedure as the linear structure. The central circular aperture diameter in the bullseye structure is 150 nm and the scale bar represents 4 μm. The sample orientation (ϕ) relative to the axis of the bullseye is defined in the inset. **e** and **f,** Experimentally measured Γ spectra corresponding to simulated spectra in **b** and **c**, respectively.

Figure 5 | Linewidth optimization and refractive index sensing. a, Spectral response, calculated using the interference model of equation (3) (dashed lines) and full-field FDTD simulations (solid lines), of a linewidth optimized aperiodic slit-groove device using Ag as the substrate upon illumination with a TM polarized light at $\theta = 0°$. The relative transmission (Γ) exhibits a peak at 540 nm with a linewidth of 14.1 nm corresponding to a resonance quality factor of ≈ 38. **b,** Top-down SEM image of the optimized device fabricated using the procedure outlined in Supplementary Figure 6 along with the model predicted surface

cross-section profile of the optimized device at a Ag-air interface. Scale bar represents 2 μm. **c,** Experimentally measured spectral response as a function of increasing Al_2O_3 layer thickness, varying from 0 nm to 9 nm, for the device in **b**. Inset shows the surface cross-section profile of the optimized device with top Al_2O_3 layer. Scale bar represents 2 μm. **d,** Peak spectral shift ($\Delta\lambda$) *vs.* refractive index change (Δn) for the data in **c**, resulting in a bulk sensitivity S_b = 330 nm/RIU and a figure of merit FOM ≈ 22.3. The FOM value achieved here is comparable to that of the state-of-the-art surface plasmon resonance sensors [56].

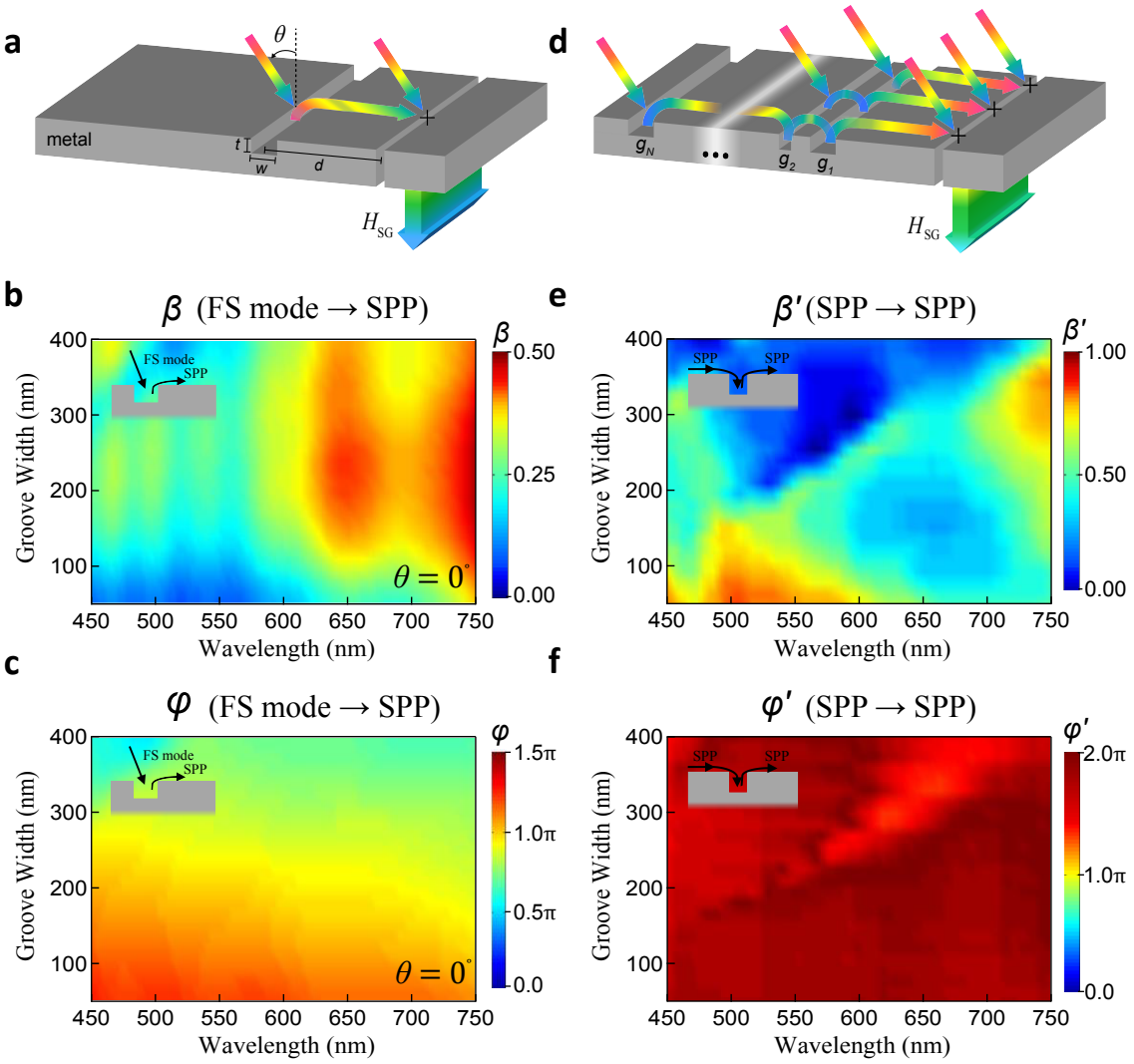
a
θ
metal
t
w
d
H_{SG}
d
g_N
g_2
g_1
H_{SG}
b
β (FS mode → SPP)
FS mode
SPP
Groove Width (nm)
Wavelength (nm)
θ = 0°
β
0.50
0.25
0.00
e
β′(SPP → SPP)
SPP
SPP
β′
1.00
0.50
0.00
c
φ (FS mode → SPP)
φ
1.5π
1.0π
0.5π
0.0
f
φ′ (SPP → SPP)
φ′
2.0π
1.0π
0.0

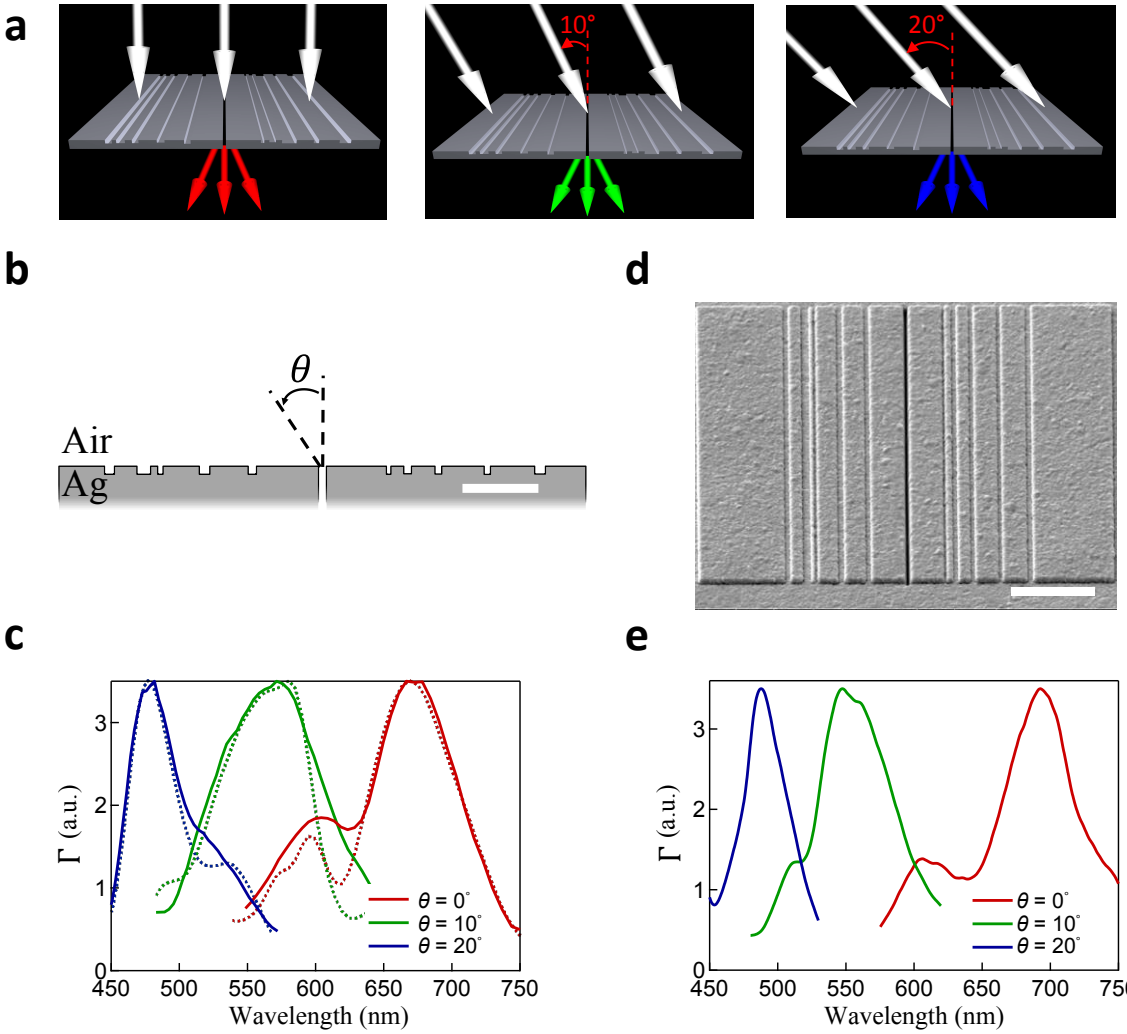
a
10°
20°
b
θ
Air
Ag
d
c
Γ (a.u.)
Wavelength (nm)
θ = 0°
θ = 10°
θ = 20°
e
Γ (a.u.)
Wavelength (nm)
θ = 0°
θ = 10°
θ = 20°

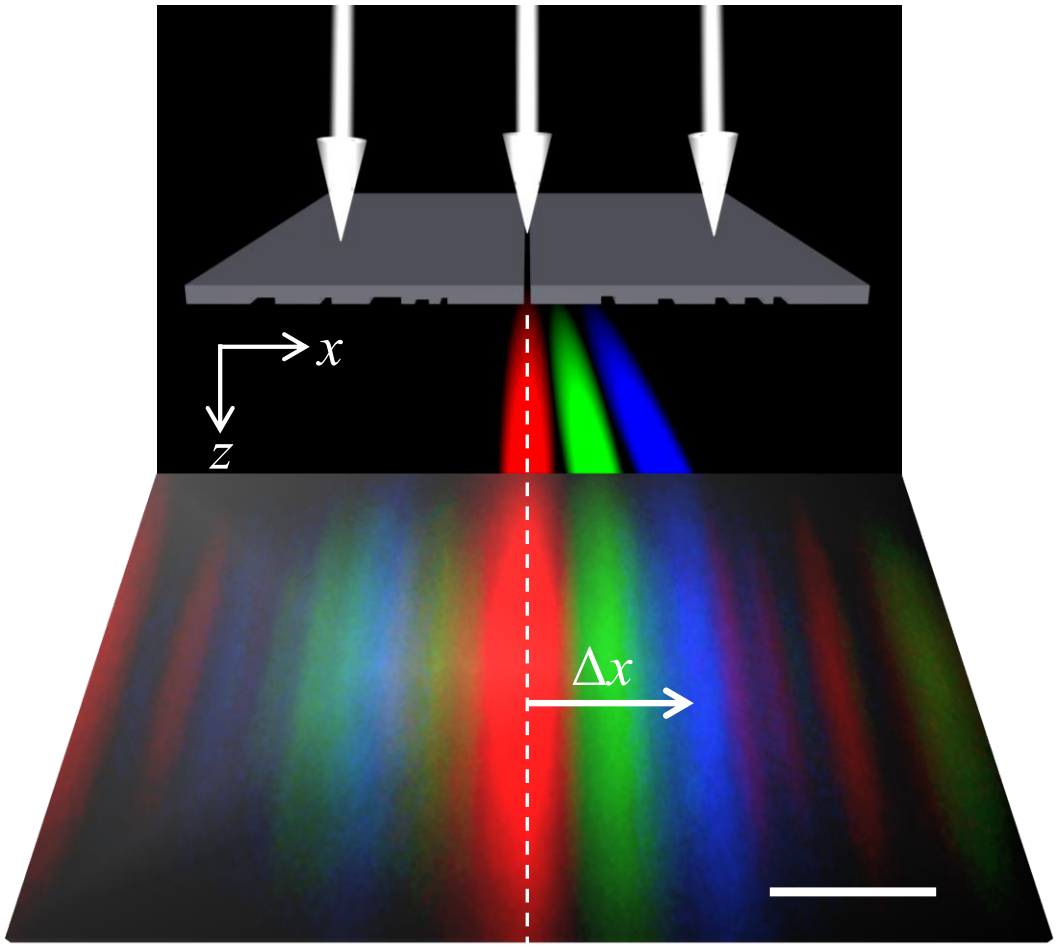
x
z
Δx

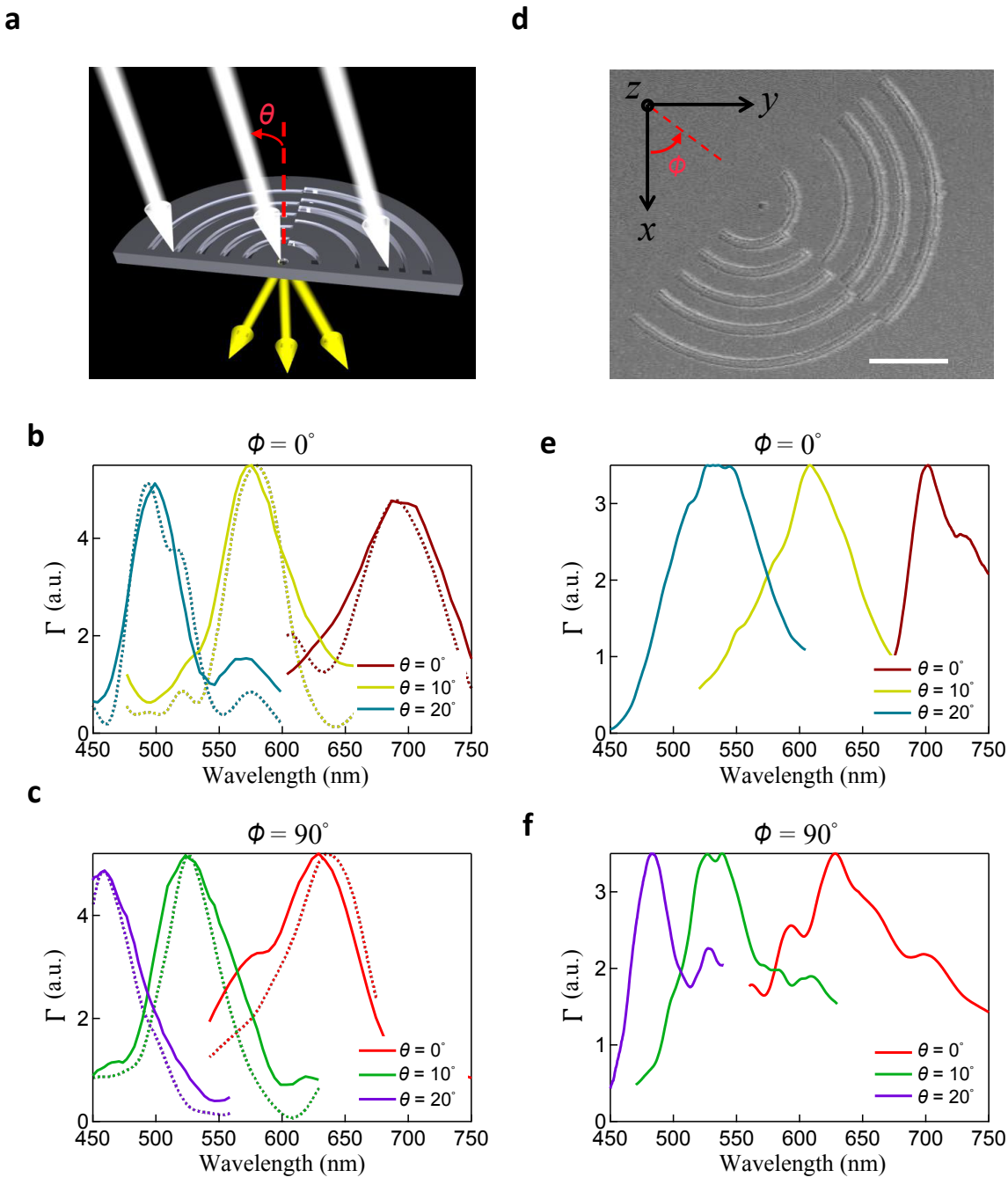
a
d
θ
z
y
x
Φ
b
e
ϕ = 0°
Γ (a.u.)
Wavelength (nm)
θ = 0°
θ = 10°
θ = 20°
c
f
ϕ = 90°

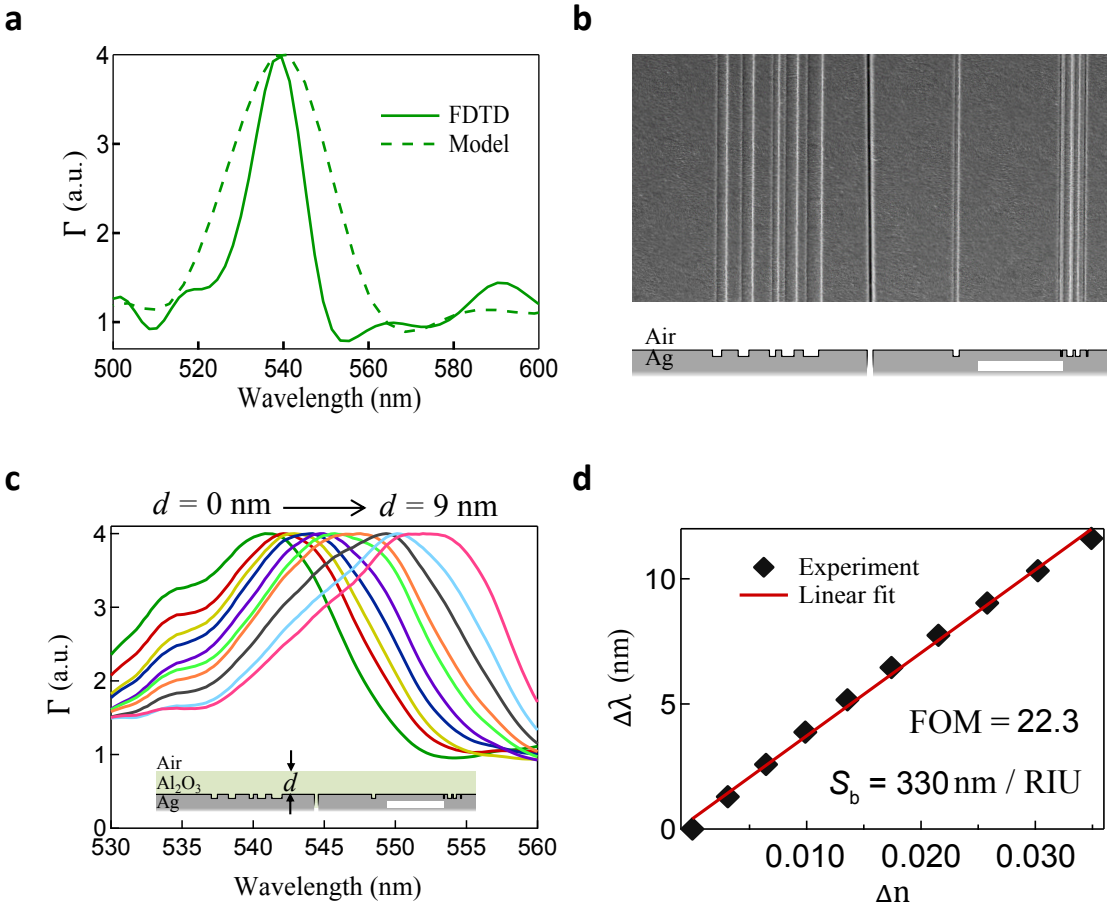
a
b
c
d
FDTD
Model
Γ (a.u.)
Wavelength (nm)
Air
Ag
d = 0 nm ⟶ d = 9 nm
Air
Al2O3
Ag
d
Experiment
Linear fit
FOM = 22.3
Sb = 330 nm / RIU
Δλ (nm)
Δn

Description of Supplementary Files

File Name: Supplementary Information

Description: Supplementary Figures, Supplementary Tables, Supplementary Notes, and Supplementary References

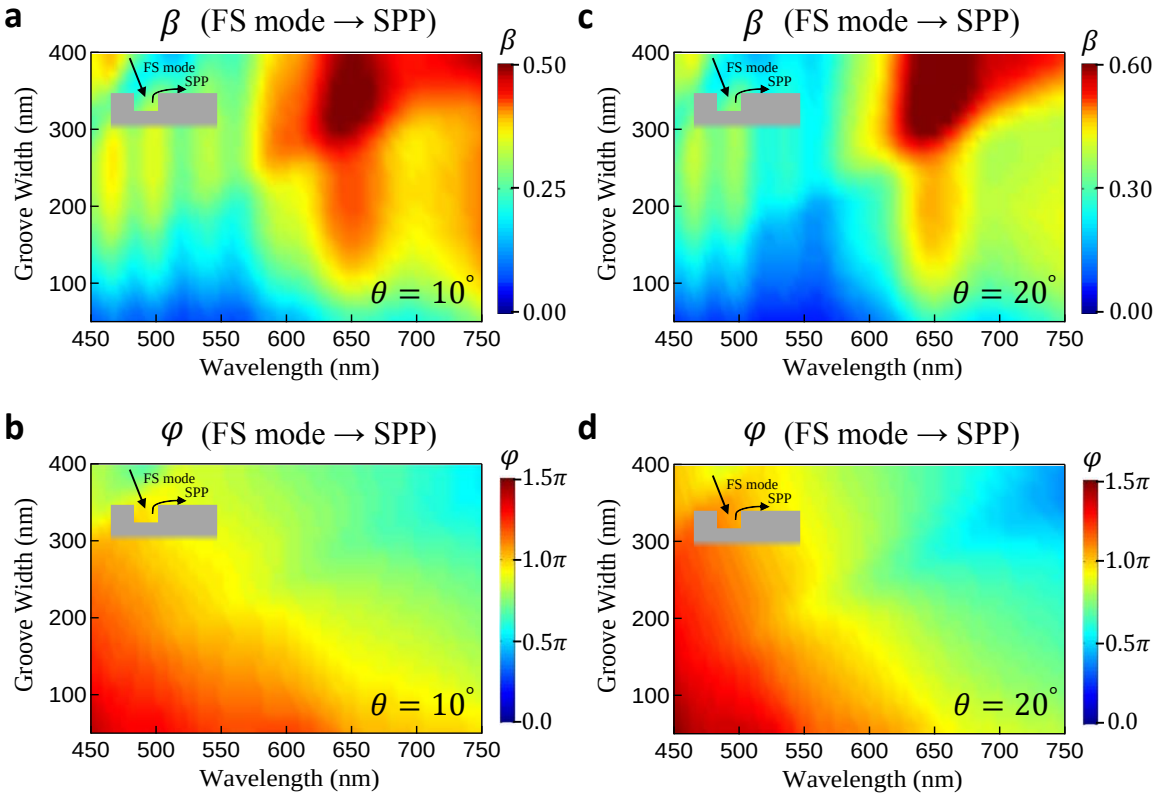

Supplementary Figure 1 | Variation in coupling coefficient β and phase shift φ with θ. Variation in β and φ as a function of both groove-width (w: 50 nm to 400 nm) and free-space wavelength (λ_0: 450 nm to 750 nm), for illumination at $\theta = 10°$ (**a** and **b,** respectively) and $\theta = 20°$ (**c** and **d,** respectively), and fixed groove-depth ($t = 100$ nm) at a Ag-air interface. The variation in β, φ, β' and φ' at $\theta = 0°$ is summarized in Figure 1 of the manuscript and, for consistency, it was verified that β' and φ' does not vary with θ.

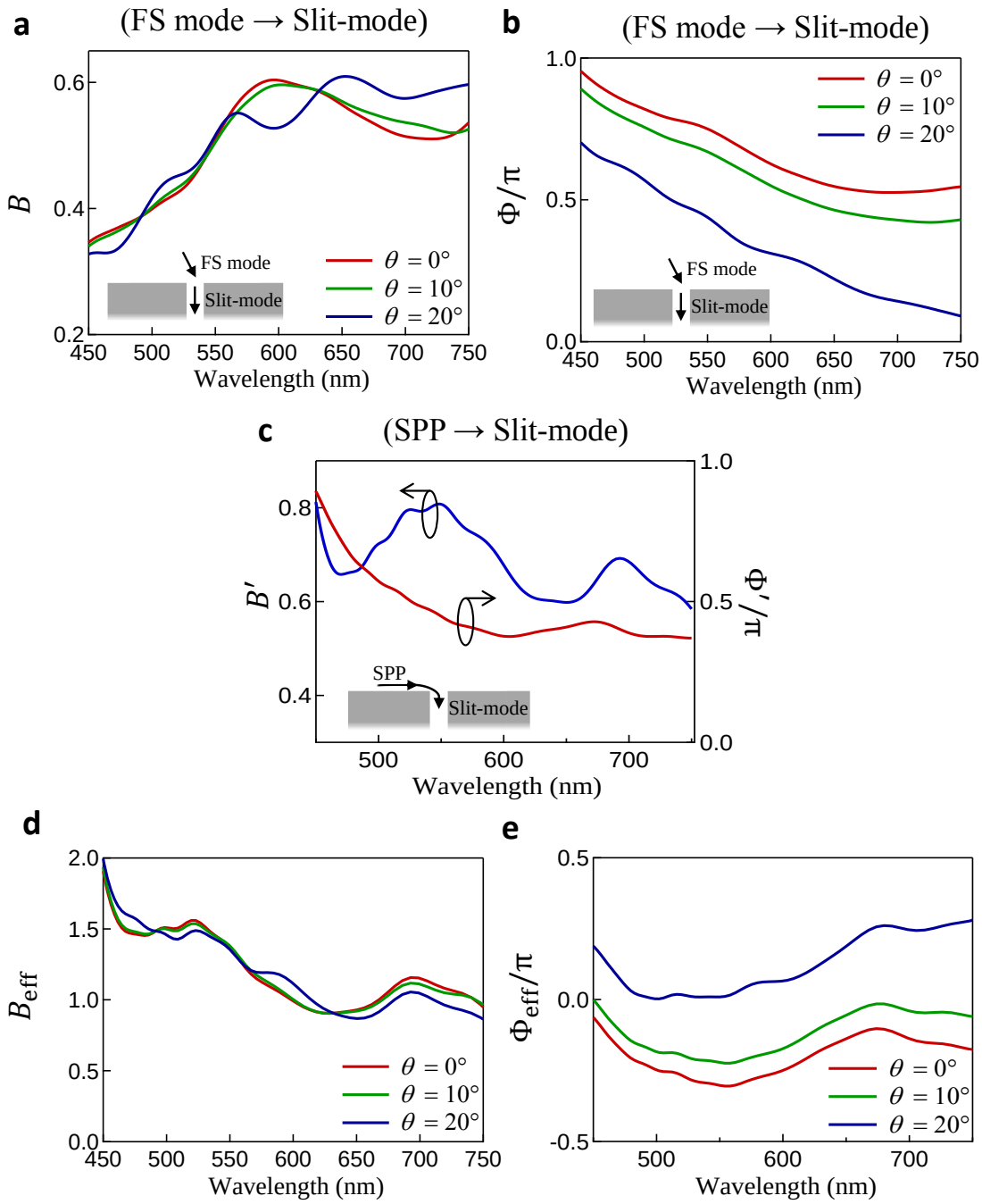

Supplementary Figure 2 | Coupling of free-space mode and SPP into a slit-mode. Variation in **a,** amplitude coupling coefficient $B(W, \theta, \lambda_0)$ and **b,** phase shift $\Phi(W, \theta, \lambda_0)$ for a plane wave coupling into guided modes inside a slit of width W = 100 nm at a Ag-air interface for λ_0 = 450 nm to 750 nm at illumination angles of $\theta = 0°$, 10° and 20°. Variations in **c,** coupling coefficient $B'(W, \lambda_0)$ and phase-shift $\Phi'(W, \lambda_0)$ for SPP modes coupling into a guided mode inside a slit of the same width. Corresponding variations in the calculated values of **d,** B_{eff} and **e,** Φ_{eff} under identical illumination conditions.

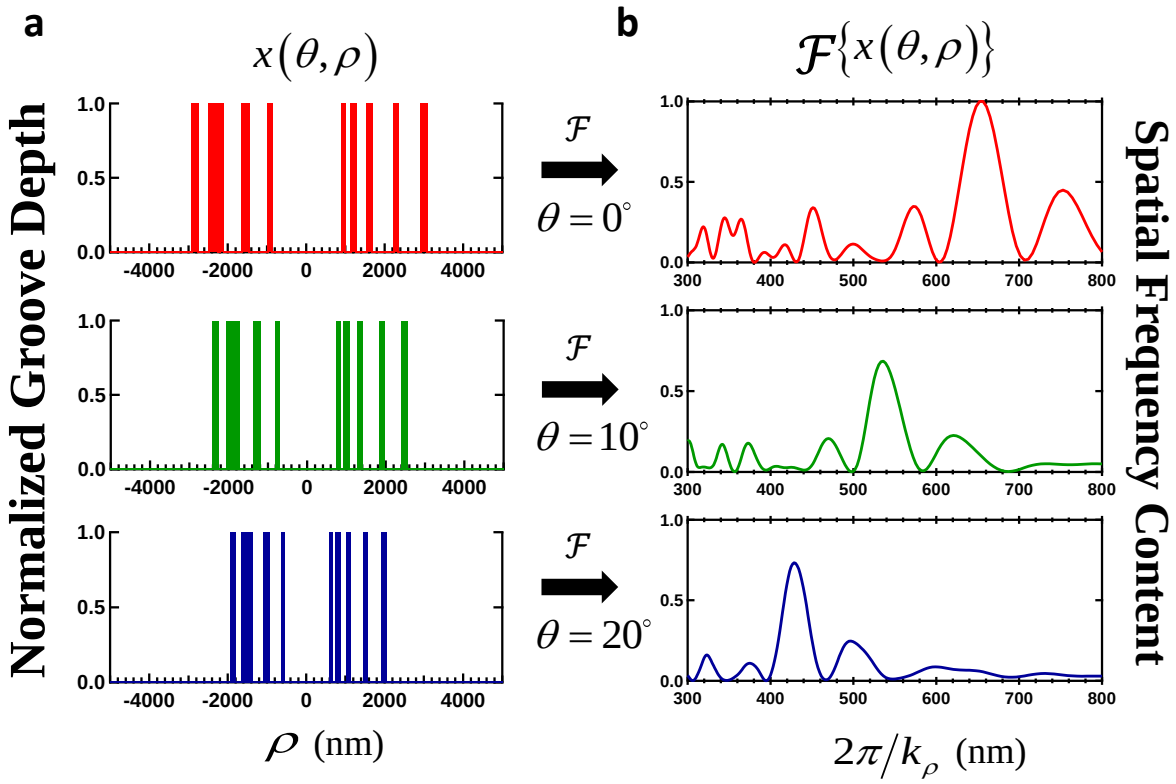

Supplementary Figure 3 | Spatial-frequency content of the aperiodic colour-filtering device. **a,** The real-space waveform representing the groove locations ρ, and their widths w, as projected onto the plane of incidence at each of the three angles of incidence (θ = 0°, 10° and 20°), for the aperiodic colour-filter device described in Figure 2 of the manuscript. As the angle of incidence θ increases, the perceived groove location and width of the aperiodic groove array varies as $\rho_{\text{eff}} = \rho(1 - \sin\theta)$ and $w_{\text{eff}} = w(1 - \sin\theta)$ respectively. **b,** Spatial Fourier-transform of the real-space groove-waveform depicting the associated reciprocal wave-vectors in inverse *k*-space. As expected, the aperiodic device exhibits dominant spatial-frequency content at wavelengths that agree with the modeled and experimentally measured spectral outputs (Figure 2c and 2e of the manuscript, respectively).

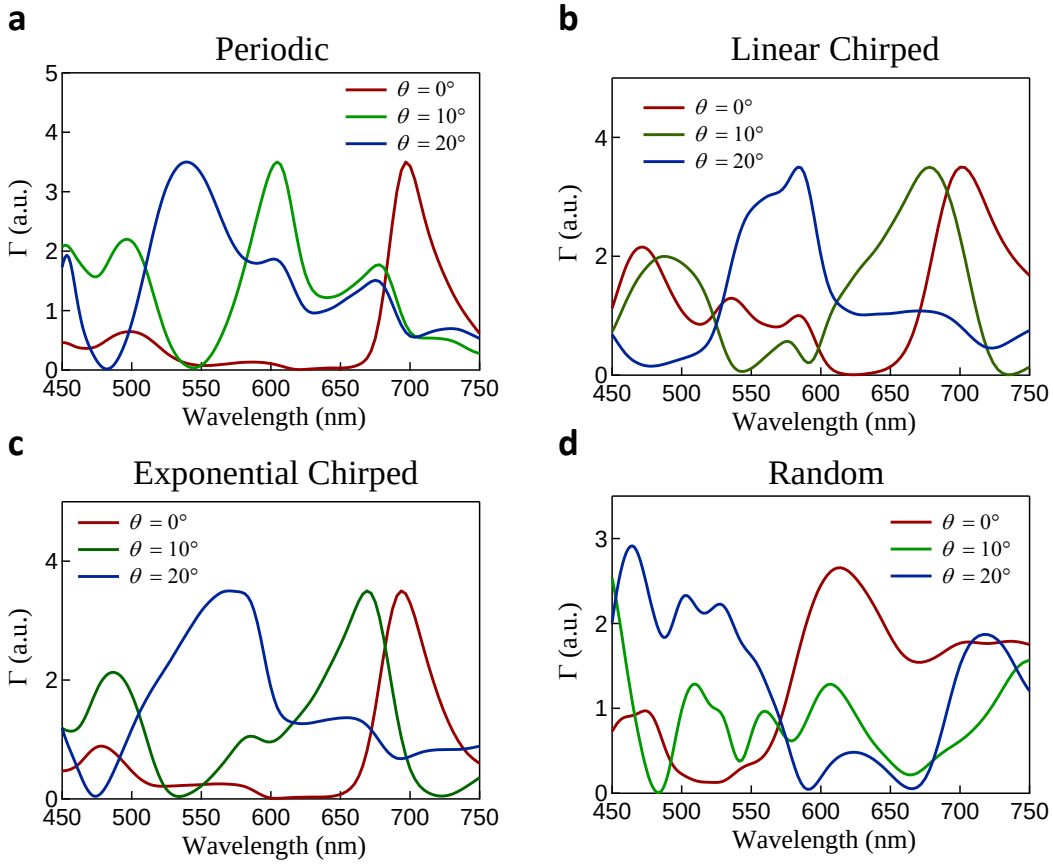

Supplementary Figure 4 | Incident-angle dependent transmission spectra for periodic, chirped and random slit-groove devices. FDTD calculated relative transmission spectra (Γ), at incident angles $\theta = 0°$, 10° and 20°, for slit-groove devices where the grooves are arranged: **a,** periodically with pitch p = 630 nm; **b,** in a linear chirped geometry; and **c,** in an exponential chirped geometry around a central subwavelength slit. For the linear chirped device, the distance of each individual groove from the slit, x_n, follows the equation: $x_n = x_{n-1} + 2\pi/k_x$ where $n > 0$, $k_x = 2\pi/x_0 + 0.0005n$ and $x_0 = 630$ nm. For the exponentially chirped device: $x_n = x_{n-1} + 2\pi/k_x$ where $n > 0$, $k_x = (1.01)^n (2\pi/x_0)$ and $x_0 = 620$ nm. **d,** Relative transmission spectra (Γ), at incident angles $\theta = 0°$, 10° and 20°, for a device with random placement of ten grooves within the 10 μm-wide lateral footprint of the device. For each simulated device, Ag-film thickness $h = 250$ nm, slit-width $W = 100$ nm, groove width $w = 50$ nm and groove depth $t = 50$ nm was used.

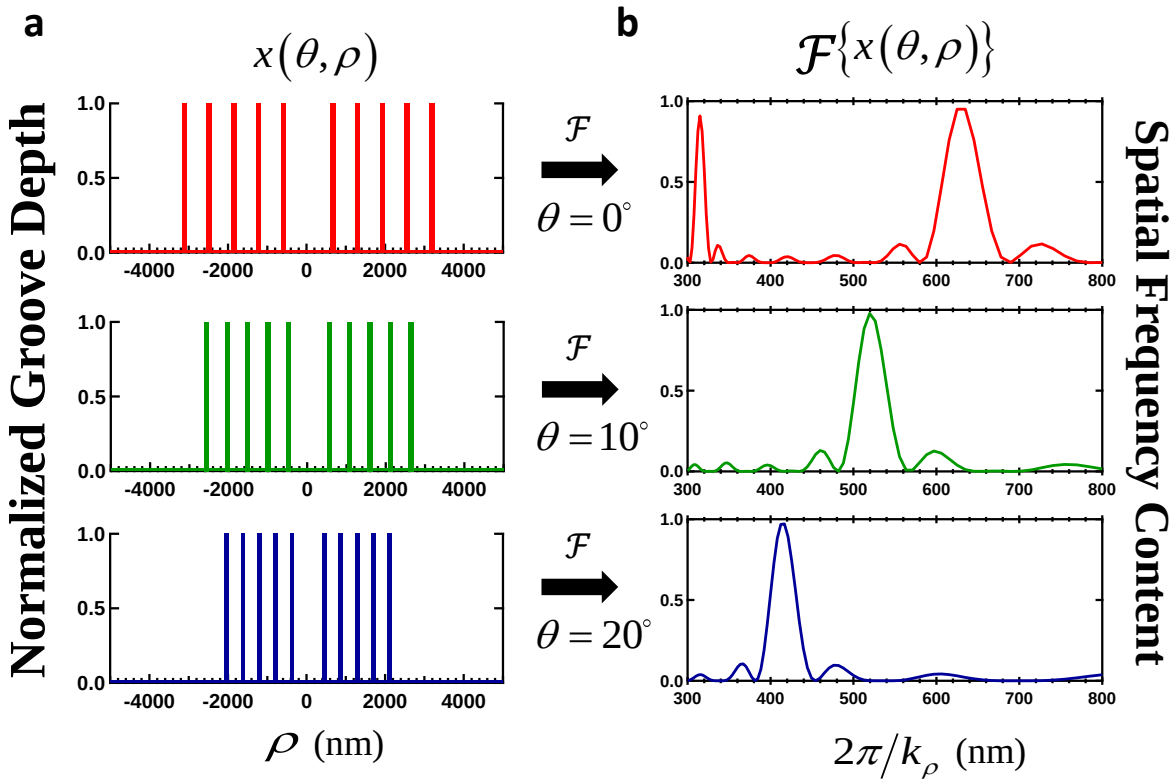

Supplementary Figure 5 | Spatial-frequency content of an equivalent periodic groove device. **a,** The real-space waveform representing the groove locations ρ, and their widths w, as projected onto the plane of incidence at each of the three angles of incidence (θ = 0°, 10° and 20°) for a periodic groove device of periodicity p = 630 nm and constant groove width W = 50 nm. As the angle of incidence θ increases, the perceived groove location and width of the periodic groove array device also varies as $\rho_{\text{eff}} = \rho(1 - \sin\theta)$ and $w_{\text{eff}} = w(1 - \sin\theta)$ respectively. **b,** Spatial Fourier-transform of the real-space groove-waveform depicting the associated reciprocal wave-vectors in inverse ***k***-space.

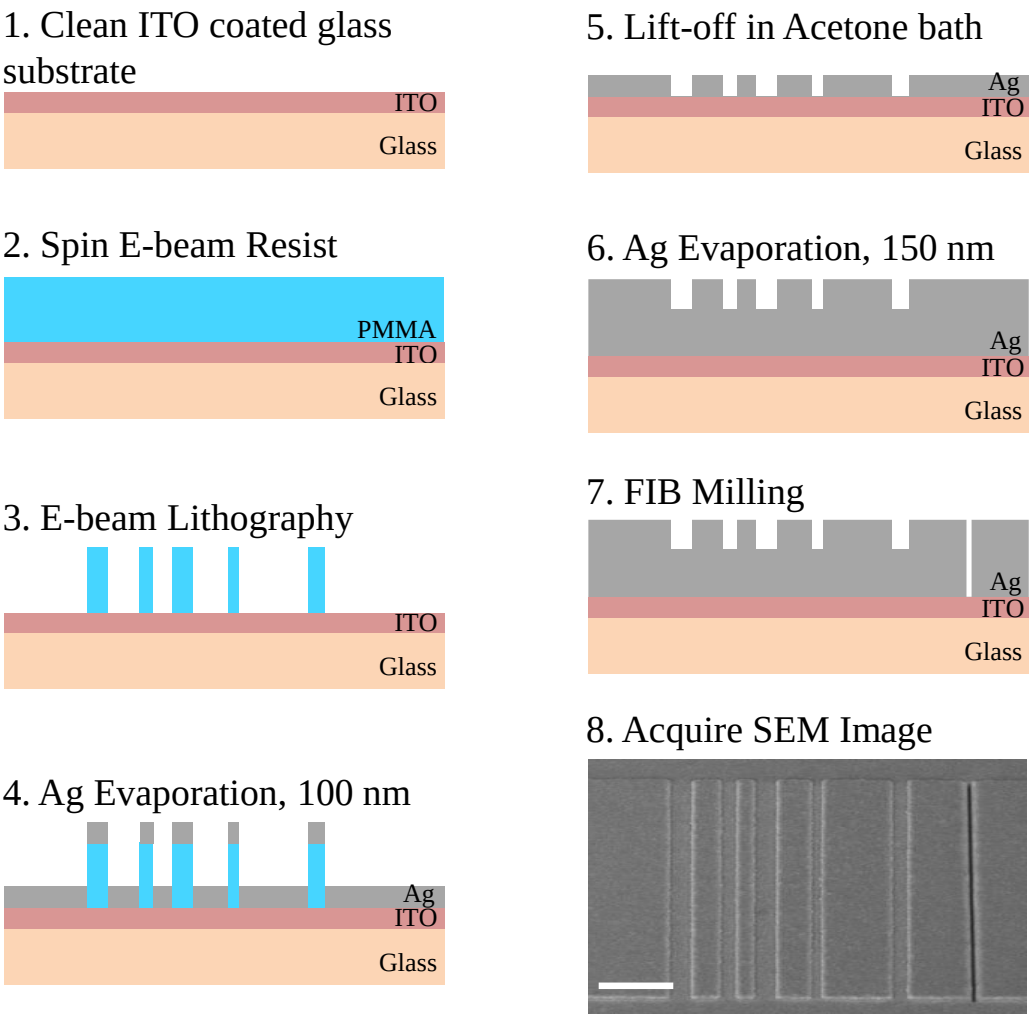

Supplementary Figure 6 | Nanofabrication process steps. E-beam resist (PMMA) was spin-coated on a pre-cleaned 20 nm thick ITO-coated fused silica substrate. E-beam lithography (at 100 keV) was used to expose the inverse groove pattern on the resist, and the exposed resist was subsequently developed for 60 s in MIBK followed by 30 s rinse in IPA. Using E-beam evaporation, a 5 nm thick Cr adhesion layer, followed by 100 nm thick Ag was deposited. Following deposition, lift-off was carried out by soaking the sample in Acetone for twelve-hours. The lift-off procedure leaves Ag islands at the location of the exposed regions. A second Ag deposition of thickness 150 nm was performed using electron-beam evaporation in order to elevate the groove pattern by an optically thick layer above the plane of the substrate. Finally, focused-ion-beam milling was used to create a 100 nm-wide, 10 μm-long central through slits (or 150 nm-diameter circular through apertures). The scale bar in the SEM image represents 2 μm.

Supplementary Note 1 | Plasmonic colour pixel analysis:

The optical contrast I_C of the aperiodic slit-groove device summarized in Figure 2 of the manuscript for the three spectral peaks with FWHM linewidths ($\Delta\lambda_{1/2}$) is calculated as:

$$I_C = \frac{I_{ON} - I_{OFF}}{I_{ON} + I_{OFF}}, \quad (1)$$

where I_{ON} represents the spectral amplitude at the targeted wavelength of interest at corresponding incident angle (for *e.g.*, 690 nm at 0°) and I_{OFF} is the residual spectral amplitude at that same wavelength (690 nm) for other incident angles (10° and 20°). The device exhibits an optical contrast of up to 93 % and linewidths as narrow as 60 nm (Supplementary Table 1).

The angle-resolved spectral colour filtering property of the aperiodic plasmonic device has potential for applications as RGB colour pixels. In recent years, several periodic plasmonic colour-pixel designs that include array of apertures, slits or slit-grooves have been proposed for high-quality CMOS digital image sensor applications [1-4]. Here, we quantitatively measure the spectral crosstalk, or bleed, which is a measure of the performance of a colour-filter, for the aperiodic angle-resolved colour-filters fabricated in this study (Figure 2 of the manuscript). Spectral crosstalk is a quantitative measurement of the overlap between various spectra in a device with a multi-band spectral response, and is defined as [4, 5]

$$C_i/C_j = \left\{ \int_{\Delta\lambda_i} \Gamma(\theta_j, \lambda_j)\, d\lambda \Big/ \int_{\Delta\lambda_i} \Gamma(\theta_i, \lambda_i)\, d\lambda \right\}_{i \neq j}, \quad (2)$$

where $\Delta\lambda_i$ is the integration range extending over the linewidth $\Delta\lambda_{1/2}$ for a relative spectral transmission $\Gamma(\theta, \lambda)$ peak at λ_i. Each integrated spectral range is represented by $C_{i/j}$ with i and j =1, 2 or 3 for the three-peaks, respectively and $i \neq j$. The ideal spectral crosstalk for a colour-pixel, given by equation (2), is 0 % – indicating that there is no spectral overlap between neighboring spectral peaks. The aperiodic plasmonic device studied here is able to achieve spectral crosstalk values that are comparable to conventional colour filters (Supplementary Table 2). Note here that the performance specifications of the experimentally implemented aperiodic colour-filter structuresincluding spectral linewidth, optical contrast and spectral

crosstalk, are all comparable to state-of-the-art plasmonic counterparts that rely on periodic nanostructures [6-8]. The optimization algorithm incorporating the interference model allows us to achieve angle resolved full-colour response from a single-pixel device on a micron-scale device footprint.

	$\Delta\lambda_{1/2}$, FWHM	I_C (690 nm, 0°)	I_C (545 nm, 10°)	I_C (480 nm, 20°)
(690 nm, 0°)	60 (120) nm	N/A	60 (87) %	93 (70) %
(545 nm, 10°)	60 (85) nm	80 (93) %	N/A	84 (95) %
(480 nm, 20°)	38 (55) nm	74 (72) %	83 (88) %	N/A

Supplementary Table 1 | Linewidth and optical contrast of the aperiodic color filter. Experimentally measured spectral peak characteristics (linewidth $\Delta\lambda_{1/2}$ and optical contrast I_C) for the aperiodic colour filter device at θ = 0°, 10° and 20° corresponding to spectral peaks at λ = 690 nm, 545 nm and 480 nm. The values predicted by FDTD-calculations are shown in parenthesis for reference.

	Red (690 nm)	Green (545 nm)	Blue (480 nm)
Red (690 nm)	N/A	10 (5)	15 (6)
Green (545 nm)	15 (9)	N/A	14 (32)
Blue (480 nm)	29 (0)	16 (17)	N/A

Supplementary Table 2 | Spectral crosstalk exhibited by the aperiodic color filter. Experimentally measured spectral crosstalk exhibited by the aperiodic colour filter along with the crosstalk values for conventional filters shown in parentheses [2].

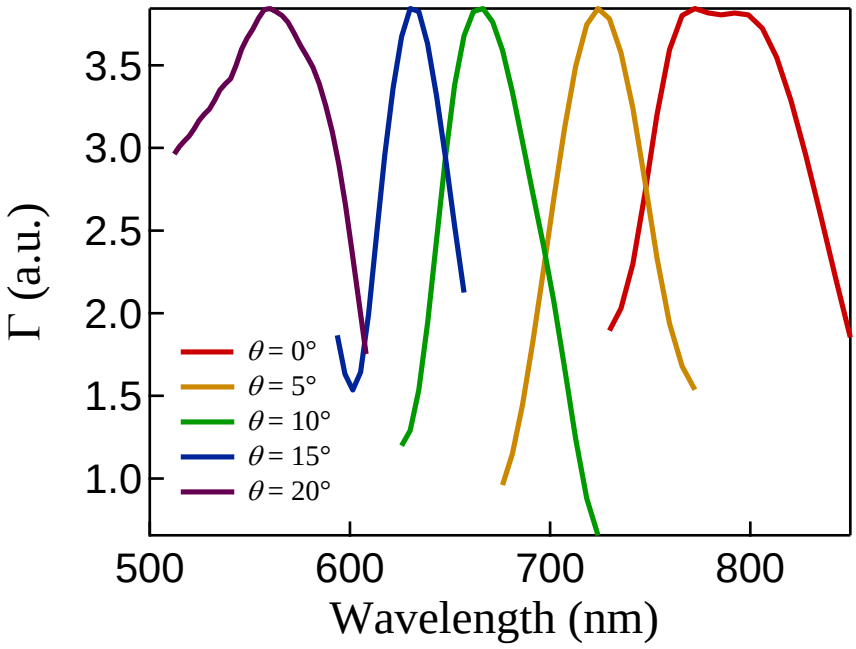

Supplementary Figure 7 | Multispectral Plasmonic Response. An aperiodic device designed on Au to exhibit five angle-dependent spectral peaks spanning the visible-near infrared spectral range. The simultaneous multi-band spectral response from a micron-scale single-pixel size device suggests application for spectral colour-sorters in areas such as multiplexed sensing or hyperspectral imaging.

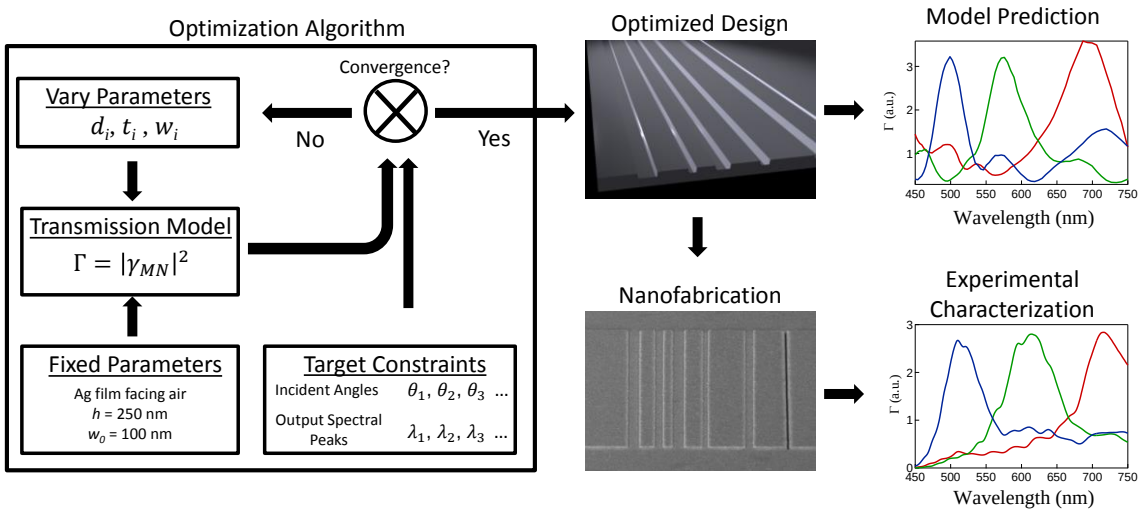

Supplementary Figure 8 | Design and implementation process summary. The complete process-flow for the design and optimization, nanofabrication and experimental characterization of an aperiodic plasmonic device with target performance specifications. The optimization process uses the transmission model described in the manuscript along with design and target constraints to optimize for the final aperiodic groove-design. The nanofabrication procedure (outlined in Supplementary Figure 6) is used to fabricate the device, and experimental characterization using a supercontinuum white-light laser as the illumination source and a spectrometer coupled to a cooled Si-CCD, is used to measure the relative spectral transmission intensity. Finally, model calculated relative transmission spectra for the optimized device design are compared with the target specification and experimentally measured spectra.

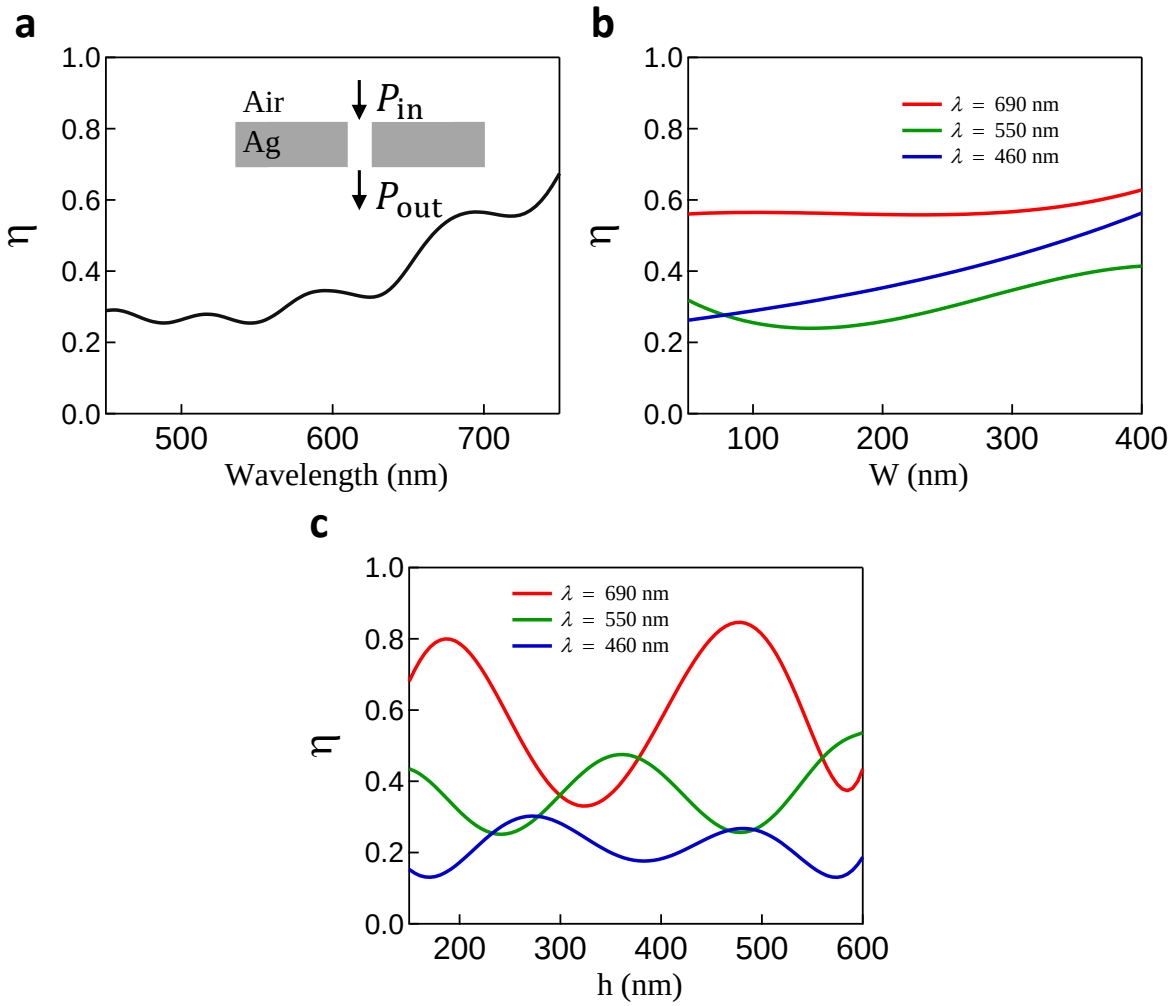

Supplementary Figure 9 | Absolute power transmission efficiency of a single-slit. a, FDTD calculated power transmission efficiency η of a single-slit of width W = 100 nm fabricated on a Ag substrate of thickness h = 250 nm. Power transmission efficiency here is defined as $\eta = P_{out}/P_{in}$ where P_{in} is the power of a normally incident TM-polarized wave on the slit and P_{out} is the power transmitted by the slit into the far-field. **b,** Variation in η as a function of W for h = 250 nm at three incident wavelengths (λ_0 = 690 nm, 550 nm and 460 nm). As expected, η increases with increasing slit-width W. **c,** Variation in η as a function of h for W = 100 nm at λ_0 = 690 nm, 550 nm and 460 nm where the oscillatory modulation in transmission *vs.* h is due to Fabry-Perot interference of the guided-mode propagating within the slit.

		$\theta = 0°$	$\theta = 10°$	$\theta = 20°$
$\phi = 0°$	Target	700 nm	600 nm	500 nm
	Model	695 nm	575 nm	495 nm
	Measured	702 nm	608 nm	535 nm
$\phi = 90°$	Target	640 nm	555 nm	460 nm
	Model	620 nm	520 nm	454 nm
	Measured	628 nm	532 nm	484 nm

Supplementary Table 3 | Designed, modeled and experimentally measured spectral peak positions. Targeted spectral-peak positions for the aperiodic bullseye structure (Figure 4 of the manuscript) under various illumination conditions, compared to the peak-positions from the interference-model for the optimized structure, and to those measured experimentally from the fabricated device.

Supplementary Note 2 | Effective index calculation of a bi-layer dielectric medium:

In order to accurately determine the figure-of-merit (FOM) of the aperiodic plasmonic sensor (studied in Figure 5 of the manuscript), an accurate determination of the effective change in refractive-index (Δn), when the metal (Ag, medium 1) surface is coated with nanometer-scale thick dielectric (Al_2O_3, medium 2) layer, is required. This is achieved by converting the bi-layer Al_2O_3/vacuum dielectric over-coating (medium 2 and 3 in Supplementary Figure 10a) into an effective bulk dielectric of refractive index n_{eff} (Supplementary Figure 10b).

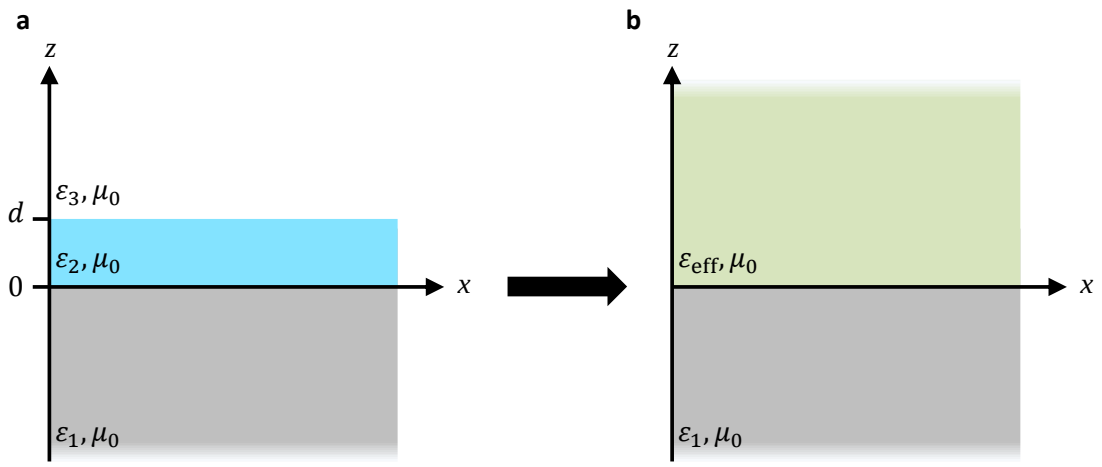

Supplementary Figure 10 | Effective medium approximation of dielectric bi-layer into a single effective dielectric medium. a, A 3-layer system. Medium 1 (described by complex dielectric permittivity ε_1 and free-space permeability μ_0) and medium 3 (ε_3, μ_0) are assumed to be of semi-infinite thickness on either side of medium 2 (ε_2, μ_0) of thickness d. All three mediums are assumed to be non-magnetic, linear, isotropic, and homogeneous. **b,** Mediums 2 and 3 together are approximated to be semi-infinite effective medium of complex dielectric permittivity ε_{eff} and free-space permeability μ_0.

The conversion requires the calculation of the lowest order bound modes in Supplementary Figure 10a. Assuming TM polarization, Ampere's law $\vec{\nabla}\times\vec{H} = -i\omega\varepsilon_0\varepsilon_j\vec{E}$ gives the full field expressions for each medium j (j =1, 2, 3). This is expressed in equations 3, 4, and 5 using Cartesian unit vectors $\hat{a}_x$, $\hat{a}_y$, and $\hat{a}_z$ where ω is the angular frequency, ε_j is the medium dielectric constant, and ε_0 the permittivity of free-space. The field amplitudes for each region are given by H_1 (region 1), $H_{2,1}, H_{2,2}$ (region 2), and H_3 (region 3). The wave-numbers for each region are given by $k_j = \sqrt{\varepsilon_j}k_0$ where $k_0 = \omega/c_0$ and c_0 is the speed of light in free-space. Each k_j obeys the relation $k_j^2 = k_{j,x}^2 + k_{j,z}^2$.

($z < 0$)

$$\vec{H}_1 = \hat{a}_y \mathrm{H}_1 e^{-ik_{1,z}z} e^{ik_{1,x}} \qquad (3.a)$$

$$\vec{E}_1 = \frac{-H_1}{\omega\varepsilon_0\varepsilon_1}\left(\hat{a}_x k_{1,z} + \hat{a}_z k_x\right) e^{-ik_{1,z}z} e^{ik_{1,x}} \qquad (3.b)$$

($0 < z < d$)

$$\vec{H}_2 = \hat{a}_y\left(\mathrm{H}_{2,1}e^{ik_{2,z}z} + \mathrm{H}_{2,2}e^{-ik_{2,z}z}\right)e^{ik_{2,x}} \tag{4.a}$$

$$\vec{E}_2 = \frac{1}{\omega\varepsilon_0\varepsilon_2}\left[\hat{a}_x k_{2,z}\left(-H_{2,1}e^{ik_{2,z}z} + H_{2,2}e^{-ik_{2,z}z}\right)e^{ik_{2,x}} - \hat{a}_z k_x\left(H_{2,1}e^{ik_{2,z}z} + H_{2,2}e^{-ik_{2,z}z}\right)e^{ik_{2,x}}\right] \tag{4.b}$$

($z > d$)

$$\vec{H}_3 = \hat{a}_y \mathrm{H}_3 e^{ik_{3,z}z}e^{ik_{3,x}} \tag{5.a}$$

$$\vec{E}_3 = \frac{H_3}{\omega\varepsilon_0\varepsilon_3}\left(-\hat{a}_x k_{3,z} + \hat{a}_z k_x\right)e^{ik_{3,z}z}e^{ik_{3,x}} \tag{5.b}$$

The boundary conditions for this system are given by:

$$\begin{aligned} H_y(z = 0^-) &= H_y(z = 0^+) \\ H_y(z = d^-) &= H_y(z = d^+) \\ E_x(z = 0^-) &= E_x(z = 0^+) \\ E_x(z = d^-) &= E_x(z = d^+) \end{aligned} \tag{6}$$

Applying these boundary conditions to equations (3), (4) and (5) gives $k_{1,x} = k_{2,x} = k_{3,x} = k_x$ and:

$$H_1 = H_{2,1} + H_{2,2} \tag{7a}$$

$$\frac{k_{1,z}}{\varepsilon_1}H_1 = \frac{k_{2,z}}{\varepsilon_2}\left(H_{2,1} - H_{2,2}\right) \tag{7b}$$

$$H_3 e^{ik_{3,z}d} = H_{2,1}e^{ik_{2,z}d} + H_{2,2}e^{-ik_{2,z}d} \tag{7c}$$

$$\frac{k_{3,z}}{\varepsilon_3}H_3 e^{ik_{3,z}d} = \frac{k_{2,z}}{\varepsilon_2}\left(-H_{2,1}e^{ik_{2,z}} + H_{2,2}e^{-ik_{2,z}}\right) \tag{7d}$$

Eliminating the four *H*-field amplitudes from equations (7a) to (7d) gives the dispersion relation:

$$e^{i2k_{2,z}d} = \frac{\left(\frac{k_{3,z}}{\varepsilon_3}+\frac{k_{2,z}}{\varepsilon_2}\right)\left(\frac{k_{1,z}}{\varepsilon_1}+\frac{k_{2,z}}{\varepsilon_2}\right)}{\left(\frac{k_{3,z}}{\varepsilon_3}-\frac{k_{2,z}}{\varepsilon_2}\right)\left(\frac{k_{1,z}}{\varepsilon_1}-\frac{k_{2,z}}{\varepsilon_2}\right)} \tag{8}$$

A similar dispersion relation is obtained in [9], however, in equation (8) no initial assumptions about k_z in the three-regions is made.

Supplementary Table 4 shows the solutions of equation (8) for various medium 2 thicknesses d, ranging from $d = 0$ nm to $d \to \infty$. For the aperiodic sensing device (in Figure 5 of the manuscript): medium 1 is Ag, medium 2 is Al_2O_3, and medium 3 is free-space. At the sensor operating wavelength of 540 nm, this corresponds to $\varepsilon_1 = -10.5760 + 0.8383i$, $\varepsilon_2 = 3.1364$, and $\varepsilon_3 = 1$, using published values of dielectric constant for Ag [10]. For $d = 0$ nm, medium 2 makes no contribution and the values of $k_{1,z}$ and $k_{3,z}$ that satisfy equation (8) are complex and represent a bound-mode (Supplementary Table 4). The calculated value for k_x (Supplementary Table 4) also agrees with the theoretical prediction for a bound SPP-mode in a two-layer metallo-dielectric system, $k_x/k_0 = \sqrt{\varepsilon_1\varepsilon_3/(\varepsilon_1 + \varepsilon_3)} = 1.0505$ [11]. In the limit $d \to \infty$, medium 3 makes no contribution, and the values of $k_{2,z}$ that satisfies equation (8) is large and imaginary. The calculated mode for k_x (Supplementary Table 4) in this case also agrees with the theoretical prediction $k_x/k_0 = \sqrt{\varepsilon_1\varepsilon_2/(\varepsilon_1 + \varepsilon_2)} = 2.1079$ [11]. For intermediate values of d, an effective medium dielectric constant can be calculated by setting $k_x/k_0 = \sqrt{\varepsilon_1\varepsilon_{\text{eff}}/(\varepsilon_1 + \varepsilon_{\text{eff}})}$. Recognizing that the refractive index of a non-magnetic, isotropic medium is given by $n_j = \sqrt{\varepsilon_j}$ gives $k_x/k_0 = n_1 n_{\text{eff}}/\sqrt{n_1^2 + n_{\text{eff}}^2}$, and so:

$$n_{\text{eff}} = \frac{n_1\left(k_x/k_0\right)}{\sqrt{n_1^2 - \left(k_x/k_0\right)^2}} \qquad (9)$$

The refractive index values for Al_2O_3 and free-space at 540 nm are $n_2 = 1.7701$ and $n_3 = 1$, respectively. Using equation (9), Supplementary Table 4 shows excellent agreement with the expected values for n_{eff} in the limiting cases of $d = 0$ nm and $d \to \infty$. Using the experimental values for the wavelength shift and linewidths (from Figure 5c of the manuscript) and the data in Supplementary Table 4, the bulk sensitivity and FOM can be directly calculated.

d (nm)	$k_{1,z}/k_0$	$k_{2,z}/k_0$	$k_{3,z}/k_0$	k_x/k_0	$Real\{n_{\mathrm{eff}}\}$
0	0.1226+3.4198i	1.4257	0.3223i	1.0506	1.0000
1	0.1225+3.4209i	1.4230	0.3338i	1.0542	1.0031
2	0.1225+3.4221i	1.4202	0.3456i	1.0580	1.0066
3	0.1224+3.4233i	1.4172	0.3577i	1.0620	1.0099
4	0.1224+3.4246i	1.4140	0.3700i	1.0662	1.0135
5	0.1223+3.4260i	1.4107	0.3825i	1.0706	1.0172
6	0.1223+3.4274i	1.4071	0.3954i	1.0753	1.0213
7	0.1222+3.4290i	1.4034	0.4086i	1.0802	1.0255
8	0.1222+3.4306i	1.3994	0.4219i	1.0853	1.0298
9	0.1221+3.4323i	1.3952	0.4356i	1.0907	1.0344
⋮	⋮	⋮	⋮	⋮	⋮
60	0.1131+3.7047i	0.0101	1.4616i	1.7709	1.5562
70	0.1118+3.7483i	0.5700i	1.5688i	1.8604	1.6159
⋮	⋮	⋮	⋮	⋮	⋮
$d \to \infty$	0.1081+3.8777i	1.1457i	1.8571i	2.1092	1.7709

Supplementary Table 4 | Effective refractive index of a bilayer dielectric medium surrounding a metal film. Effective index n_{eff} *vs*. dielectric layer thickness d (medium 2) for the three-layer system shown in Supplementary Figure 10a assuming medium 1 to be silver Ag, medium 2 to be Al_2O_3, and medium 3 to be free-space.

Supplementary Note 3 | Refractive index sensing:

In addition to demonstrating the versatility of the optimization algorithm, incorporating the interference model, to perform linewidth optimization necessary for sensing applications at any arbitrary wavelength and angle of incidence (Figure 5 of the manuscript), we summarize here the sensing capabilities of the multi-spectral response of an aperiodic device designed on Au-film for operation spanning the visible wavelengths. Simultaneous illumination of the sample at multiple angles of incidence would result in multiple discrete pre-defined spectral peaks in transmission thereby allowing for multiplexed sensing capabilities, which can result in higher-sensitivity than is possible from devices that exhibits only one spectral peak [12]. The aperiodic Au device was designed to fit within the same lateral foot-print as the Ag aperiodic slit-groove device ($\leq$ 10 μm), and is theoretically implemented here to exhibit spectral peaks at 790 nm, 725 nm, 665 nm, 630 nm, and 560 nm for incident angles 0°, 5°, 10°, 15° and 20°, respectively, (Supplementary Figure 7). As the refractive index of the medium surrounding the patterned side of the device is varied from 1.00 to 1.02, each of the five-spectral peaks were found to red-shift with comparable index-sensitivities. Representative spectral-shifts as a function of change in refractive index for two spectral peaks corresponding to angles of incidence of θ = 5° and 15° are shown in Supplementary Figure 11a, and the device sensitivity response is plotted in Supplementary Figure 11b. For the Au multi-band device operating at θ = 0°, the bulk sensitivity is calculated to be S_b = 532 nm/RIU. Combining this with the resonance linewidth of $\Delta\lambda_{1/2}$ = 24 nm at λ_i = 615 nm gives a figure-of-merit, FOM = 22. For other angles of incidence, the FOM values are 35, 42, 25, and 25 at θ = 5°, 10°, 15° and 20°, respectively. These FOM values for the multiband structure over multiple angles of incidence are comparable to the typical values for plasmonic sensors [12-16].

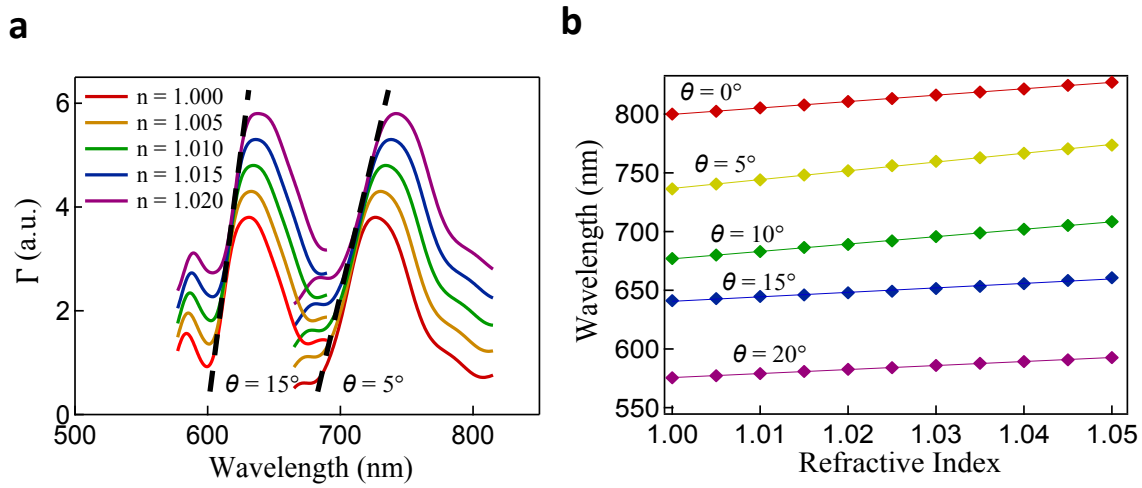

Supplementary Figure 11 | Multiplexed plasmonic sensing. a, Representative shift in spectral response of the five-peak Au device (shown in Supplementary Figure 7) as a function of change in refractive index of the surrounding media when illuminated at multiple angles of incidence (θ = 5° and 15°). The spectra in **a** are offset vertically for clarity. **b,** Summary of the shift in spectral peak as a function of change in refractive index for the Au slit-groove array devices at the five pre-defined angles of incidence. The slope of each curve corresponds to the index-sensitivity of the device which in conjunction with linewidth is used to calculate the FOM.

Supplementary Note 4 | SPP propagation length and Ag degradation:

The SPP propagation decay length L_{SPP} is experimentally measured (using the method described in ref. 17) to be ≈ 7 μm at λ_0 = 690 nm on an evaporated Ag-air interface used in the manuscript (Supplementary Figure 12, blue squares). For an equivalent Ag-air interface fabricated using the template-stripping approach, the SPP propagation decay length L_{SPP} is experimentally measured to be ≈ 30 μm at λ_0 = 690 nm on an evaporated Ag-air interface used in the manuscript (Supplementary Figure 12, purple spheres), a value that closely matches the theoretical SPP decay length calculated using the bulk effective permittivity of template-stripped Ag measured by a spectroscopic ellipsometer (Supplementary Figure 12, dashed black line).

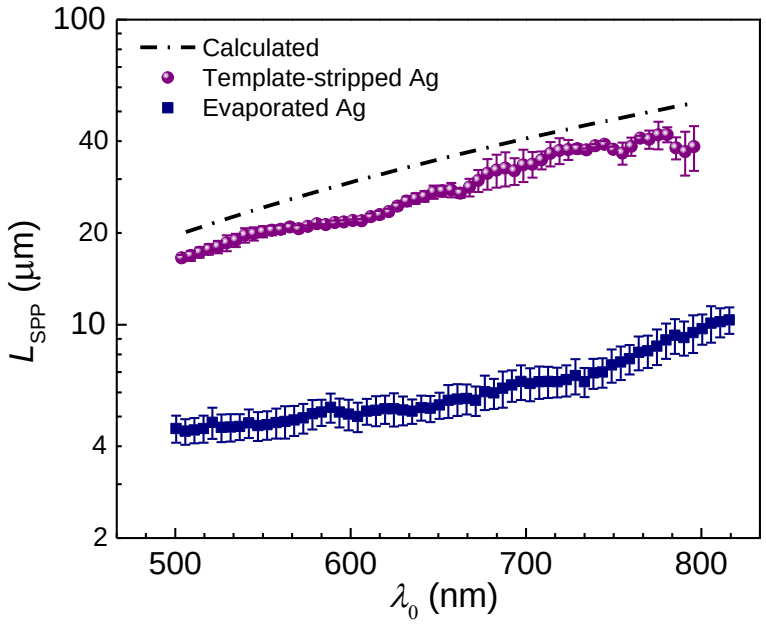

Supplementary Figure 12 | Propagation decay length of SPPs propagating on a Ag-air interface. Experimentally measured 1/e decay length L_{SPP} of SPPs for free-space wavelengths ranging from 500 nm to 800 nm on an evaporated Ag-air interface (blue squares) and a template-stripped Ag-air interface (purple spheres). The theoretical SPP decay length calculated using the bulk effective permittivity of template-stripped Ag (dashed black line).

Note that oxidation of Ag can also have a detrimental issue on device performance when operated under ambient conditions for long periods of time. We have not observed any degradation of Ag films used in our experiments as they were only exposed to air for the duration of the experiments (few minutes to an hour) and stored in a dry-environment. A few-nm thick atomic-layer-deposited protective overcoat of low-loss oxide (Al_2O_3) or use of doped-Ag films has been shown to dramatically improve the stability of Ag films without any compromise on the optical performance [18, 19].

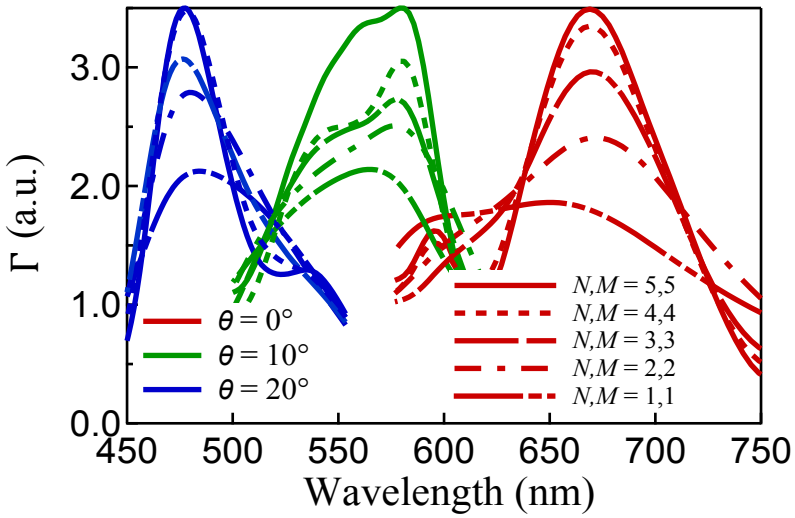

Supplementary Figure 13 | Number of Grooves Dependence. Optimized relative spectral transmission (Γ) through an aperiodic plasmonic device as a function of increasing number of grooves on both sides of the slit ($N, M = 1, 1$) to ($N, M = 5, 5$) for the three angles of incidence $\theta = 0°$, 10° and 20°.

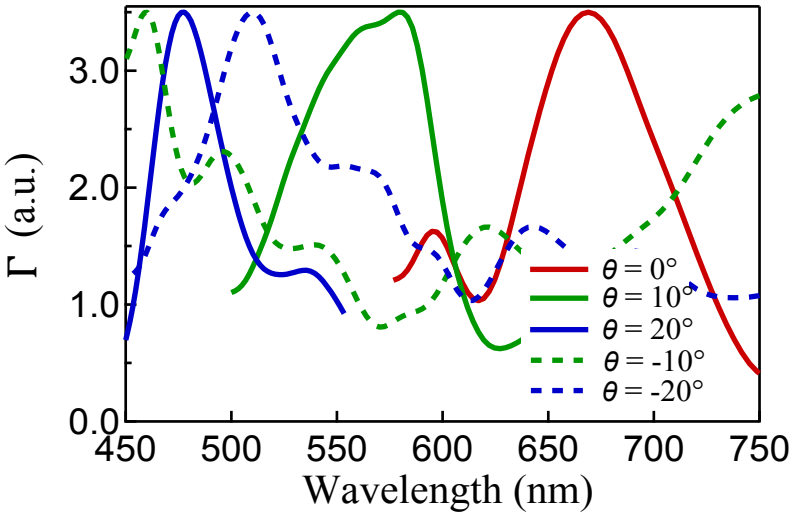

Supplementary Figure 14 | Relative transmission at off-angle incidence. Relative spectral transmission (Γ) through the aperiodic plasmonic device (Figure 2 of the manuscript) at non-optimized angles of incidence of $\theta = -10°$ and $-20°$ (dotted lines) along with the spectral transmission at optimized angles of $\theta = 0°$, 10° and 20° (solid lines).

Supplementary References:

[1] Burgos, S. P., Yokogawa, S. and Atwater, H. A. Colour imaging via nearest neighbor hole coupling in plasmonic colour filters integrated onto a complementary metal-oxide semiconductor image sensor. *ACS Nano* **7**, 10038–10047 (2013).

[2] Chen, Q., Chitnis, D., Walls, K., Drysdale, T. D., Collins, S. and Cumming, D. R. CMOS photodetectors integrated with plasmonic colour filters. *IEEE Photonics Technology Letters* **24**, 197–199 (2012).

[3] Zheng, B. Y., Wang, Y., Nordlander, P. and Halas, N. J. Colour-selective and CMOS-compatible photodetection based on Aluminum plasmonics. *Advanced Materials* **26**, 6318–6323 (2014).

[4] Yu, Y., Chen, Q., Wen, L., Hu, X. and Zhang, H. F. Spatial optical crosstalk in CMOS image sensors integrated with plasmonic colour filters. *Optics Express* **23**, 21994–22003 (2015).

[5] Agranov G., Berezin V. and Tsai R. H. Crosstalk and microlens study in a colour CMOS image sensor. *IEEE Trans. Electron. Devices* **50**, 4–11 (2003).

[6] Sounas, D. L. and Alù, A. Colour separation through spectrally-selective optical funneling. *ACS Photonics* **3**, 620−626 (2016).

[7] Li, E., Chong, X., Ren, F. and Wang, A. X. Broadband on-chip near-infrared spectroscopy based on a plasmonic grating filter array. *Optics Letters* **41**, 1913–1916 (2016).

[8] Haïdar, R., Vincent, G. G., Collin, S. P., Bardou, N., Guérineau, N., Deschamps, J. L. and Pelouard, J. L. Free-standing subwavelength metallic gratings for snapshot multispectral imaging. *Applied Physics Letters* **96**, 221104 (2010).

[9] Maier, S. A. *Plasmonics: Fundamentals and Applications*. (Springer US, 2007).

[10] Palik, E. *Handbook of optical constants of solids.* (Academic Press, New York, 1985).

[11] Raether, H. *Surface-plasmons on smooth and rough surfaces and on gratings*. *Springer Tracts in. Mod. Phys.* **111**, 1–133 (Springer, 1988).

[12] Gao, Y., Xin, Z., Gan, Q., Cheng, X. and Bartoli, F. J. Plasmonic interferometers for label-free multiplexed sensing. *Optics Express* **21**, 5859–5871 (2013).

[13] Shen, Y., Zhou, J., Liu, T., Tao, Y., Jiang, R., Liu, M., Xiao, G., Zhu, J., Zhou, Z. -K., Wang, X., Jin, C. and Wang, J. Plasmonic gold mushroom arrays with refractive index sensing figures of merit approaching the theoretical limit. *Nature Communications* **4**, 2381 (2013).

[14] Feng, J., Siu, V. S., Roelke, A., Mehta, V., Rhieu, S. Y., Palmore, G. T. R. and Pacifici, D. Nanoscale plasmonic interferometers for multispectral, high-throughput biochemical sensing. *Nano Letters* **12**, 602–609 (2012).

[15] Valsecchi, C. and Brolo, A. G. Periodic metallic nanostructures as plasmonic chemical sensors. *Langmuir* **29**, 5638–5649 (2013).

[16] Wang, X. -Y., Wang, Y. -L., Wang, S., Li, B., Zhang, X. -W., Dai, L. and Ma, R. -M. Lasing enhanced surface plasmon resonance sensing. *Nanophotonics* **5**, 52–58 (2016).

[17] Nagpal, P. Lindquist, N. C. Oh, S.-H. and Norris, D. J. Ultrasmooth patterned metals for plasmonics and metamaterials. *Science* **325**, 594–597 (2009).

[18] Zhang, X., Zhao, J., Whitney, A. V., Elam, J. W. and Van Duyne, R. P. Ultrastable substrates for surface-enhanced Raman spectroscopy: Al_2O_3 overlayers fabricated by atomic layer deposition yield improved Anthrax biomarker detection. *Journal of the American Chemical Society* **128,** 10304–10309 (2006).

[19] Zhang, C. *et al.* An Ultrathin, smooth, and low-loss Al-doped Ag film and its application as a transparent electrode in organic photovoltaics. *Advanced Materials* **26,** 5696–5701 (2014).